

Amelia: A Large Dataset and Model for Airport Surface Movement Forecasting

Ingrid Navarro* Pablo Ortega-Kral*, Jay Patrikar, Haichuan Wang, Alonso Cano, Sebastian Scherer[‡] and Jean Oh[†]
 Carnegie Mellon University, Pittsburgh PA, USA, 15213

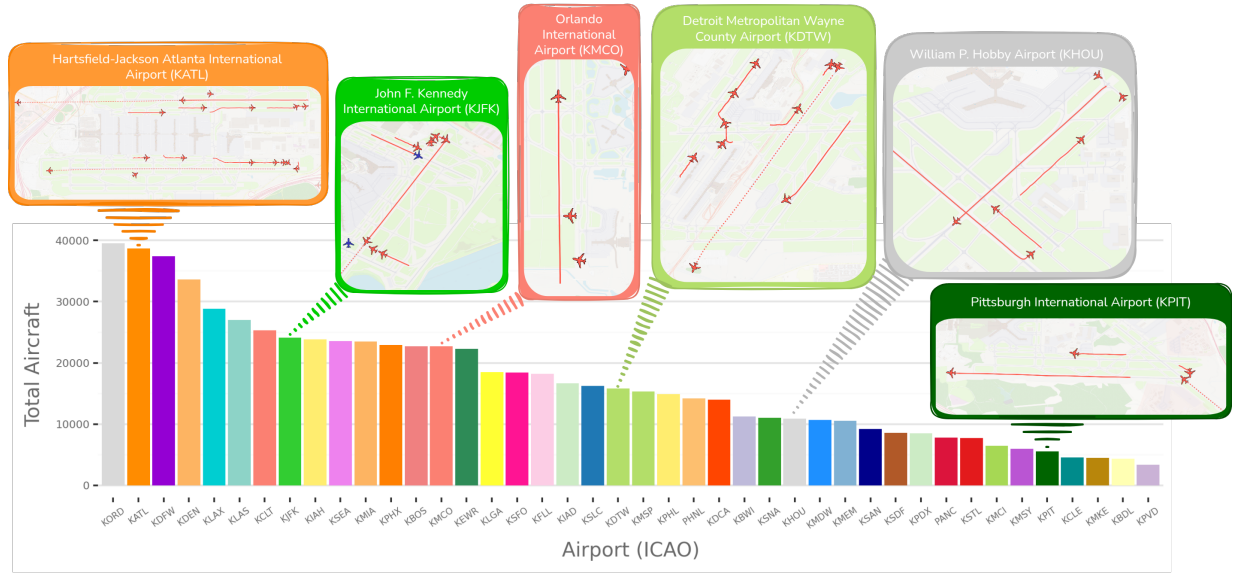


Fig. 1 The Amelia-42 Dataset. Total aircraft count per airport over a span of 15 days. We also include examples of airport scenes across multiple airports, showing diverse behaviors and interactions.

Demand for air travel is rising, straining existing aviation infrastructure. In the US, more than 90% of airport control towers are understaffed, falling short of FAA and union standards. This, in part, has contributed to an uptick in near-misses and safety-critical events, highlighting the need for advancements in air traffic management technologies to ensure safe and efficient operations. Data-driven predictive models for terminal airspace show potential to address these challenges; however, the lack of large-scale surface movement datasets in the public domain has hindered the development of scalable and generalizable approaches. To address this, we introduce *Amelia-42*, a first-of-its-kind large collection of raw airport surface movements reports streamed through the FAA’s System Wide Information Management (SWIM) Program, comprising over two years of trajectory data (~9.19TB) across 42 US airports. We open-source tools to process this data into clean tabular position reports. We release *Amelia42-Mini*, a 15-day sample per airport, fully processed data on HuggingFace for ease of use. We also present a trajectory forecasting benchmark consisting of *Amelia10-Bench*,

*Equal contribution
[†]Equal Advising

an accessible experiment family using 292 days from 10 airports, as well as Amelia-TF, a transformer-based baseline for multi-agent trajectory forecasting. All resources are available at our website: ameliacmu.github.io and huggingface.co/AmeliaCMU.

I. Introduction

In early 2023, the U.S. National Airspace System (NAS) recorded more aircraft close-calls than in the previous five years combined [1]. Poorly managed airport operations pose serious risks. For instance, in recent events, the world has witnessed major incidents that have caused significant damage and, more importantly, resulted in the loss of lives [2–4]. While part of these alarming trends stem from deficiencies within Air Traffic Control (ATC) facilities [5, 6], growing airspace demand [7] and record-setting travel volumes [8] are further straining the existing infrastructure. Moreover, the emergence of Advanced Aerial Mobility (AAM) further highlights the need for automated, data-driven decision-support systems [9] to safely integrate manned and unmanned aircraft. These challenges underscore the urgency of advancing air traffic management and aviation safety standards to mitigate potential failures and prevent catastrophic accidents.

Data-driven human-aware predictive approaches have shown great success in domains like autonomous driving [10–13] and crowd navigation [13–15], and hold significant potential for addressing **safety and efficiency** challenges in aviation. For example, they could be utilized by aircraft and management facilities to enhance situational awareness through onboard sensors for intelligent navigation [16, 17] and automated go-around decisions to prevent near misses and collisions [18–21]. They could also improve efficiency [22], for instance, by estimating taxi-out and departure times to coordinate operations [23, 24], de-icing schedules [25], and time-of-arrival estimates [26]. However, the lack of unified frameworks and large-scale open datasets has limited the **scalability and generalizability** of existing solutions [27]. Most prior works rely on small datasets [16, 28, 29] or simple prediction models that do not account for complex interactions and modalities of information [30].

To address this gap, this paper introduces the *Amelia* framework, featuring four key contributions:

First, we present *Amelia-42*, a large-scale dataset focused on airport surface operations, collected via the Federal Aviation Administration’s (FAA) System Wide Information Management (SWIM) Program. Our dataset includes over 9.19TB of compressed surface movement trajectory data from 42 U.S. airports, starting from December 1, 2022, up to today. Alongside the SWIM data, we collect, post-process, and release airport surface maps as lightweight, semantically marked graphs. Then, for ease of accessibility, we release *Amelia42-Mini*, a clean, tabular 15-day per-airport (i.e., 630 total days) sample via HuggingFace, along with tools for downloading and processing additional data as needed. To our knowledge, *Amelia-42* is the largest open dataset of its kind and is intended for use by researchers working on airport surface operations, motion forecasting, and beyond.

Second, we introduce *Amelia10-Bench*, a trajectory forecasting benchmark designed to support the research and development of large predictive models for aviation, as well as scalable and generalizable learning strategies for motion

forecasting. The benchmark covers over 290 days of data from 10 different airports and includes a family of experiments across two settings: `SingleAirport` and `MultiAirport`. The `SingleAirport` setting focuses on studying *in-domain* performance, i.e., training and testing model performance one airport at a time, while `MultiAirport` setting focuses on studying *cross-domain* generalization capabilities of predictive models.

Third, to provide baseline results across the proposed benchmark, we contribute `Amelia-TF`, a large transformer-based trajectory forecasting model, designed for predicting aircraft’s future movements by characterizing aircraft’s temporal information, and agent-to-agent and agent-to-map relationships. `Amelia-TF` leverages a novel automated scene representation strategy that abstracts and prioritizes scene information to improve model generalization. Using standard metrics for trajectory prediction, we provide both short- and long-horizon results across `Amelia10-Bench`.

Finally, along with our dataset, we also release our model, model weights, and all tools used for collection and processing to promote large-scale open aviation research at: ameliacmu.github.io and huggingface.co/AmeliaCMU

II. Related Work

Trajectory Forecasting Datasets in Aviation. In contrast to the autonomous driving (AD) domain, where large-scale datasets exist [10–13], the domain of aviation has not been studied as extensively due in part to the lack of datasets. Previous works [27] have criticized the dominance of proprietary, non-public data in aviation research, finding that 68% of the works reviewed utilized solely proprietary data. In response, `TrajAir` [31] was introduced as a dataset in the public domain for motion prediction in general aviation. It aimed to learn how pilots interact in non-towered airports but consisted only of trajectory information and focused only on a single airport. Accordingly, in response to the lack of curated large-scale publicly accessible datasets in this domain, we release the `Amelia-42` dataset in its raw format, along with two curated subsets, `Amelia42-Mini` and `Amelia10-Bench`, for ease of accessibility to researchers in the forecasting domain.

To the best of our knowledge, `Amelia-42` is the largest dataset of its kind and is geared towards use by researchers even beyond those interested in airport motion forecasting.

Trajectory Forecasting Models in Aviation. Trajectory forecasting is a well established field in autonomous driving [32–37] and crowd navigation [13, 36, 38–40]. Motivated by the growing challenges of coordinating air traffic, an emerging research area focuses on employing learning-based trajectory forecasting in the aviation domain. The bulk of prior art [41–43] targets short-horizon in-air prediction. `FlightBERT` [41] is one of the first in this line of research. It binarizes each trajectory point and feeds the resulting bit-strings to a transformer, framing forecasting as a multi-binary classification problem. Closest to our setting is [28], where the authors analyze four hours’ worth of movement at two airports, identifying the 2D position of each agent; and [44], who use one-week ADS-B data collected at Singapore Changi Airport. Neither dataset is in the public domain, and both studies are limited to a single airport, restricting



Fig. 2 The *Amelia* data pipeline. A) Raw position reports from the FAA’s SWIM Terminal Data Distribution System are continuously logged and released as *Amelia-42*, from December 2nd, 2022, to the present. B) Airport-specific geofences are defined to delimit movement areas as well as take-off and landing extensions to runways. C) Data within the geo-fence is processed into clean tabular 1-Hz position reports. D) As additional context, semantic routing graphs are created for each airport.

generalization.

Our work differs significantly in scale and scope, as we wish to forecast trajectories for airport ground operations across multiple airport topologies; a setting that current datasets and methods have not fully addressed. Single-agent models such as FlightBERT lack mechanisms to capture inter-agent interactions, as well as failing to capture contextual information that conditions different behaviors. In addition, prior works’ absolute trajectory representations can limit transfer between airports, whereas our multi-airport dataset necessitates efficient encoding for better large-scale training.

III. Dataset Collection and Processing

Surface area operations encompass landings, departures, and ground-vehicle activity within the airport movement zone. The *Amelia* framework focuses on data-driven behavior prediction within this area. To support this, we build a large-scale dataset by logging every position report that enters the zone, tracking each agent until it exits or crosses the non-movement boundary. These raw logs are then processed into tabular trajectories with agent metadata suitable for training trajectory forecasting models. The resulting data format is compatible with existing dataloaders for motion forecasting [37]. We describe our collection and processing methodologies for the trajectory data in Section III.A and map data Section III.B, with further detail in Appendix B. An overview of the data pipeline is shown in Figure 2.

A. Trajectory Data

Raw Data. *Amelia-42* leverages FAA’s SWIM* Terminal Data Distribution System (STDDs), which aggregates multiple terminal-area feeds into a single stream of position reports for aircraft and vehicles operating within a few miles of the airport, covering *approach* and *ground* movement events. Each report arrives as an XML message that we continuously stream and group into newline-delimited JSON files, compressed for storage. Our data collection started on December 1st, 2022, and continues up to today. It currently represents **over 9.19 TB** of compressed position reports

*System Wide Information Management program

recorded and stored on our in-house server.

Processed Data. Given that the raw position reports are irregularly sampled, have noise, and include many tracks outside of areas of movement, we further develop data pre-processing scripts following [31]. Here, we focus on 42 airports in the US, for which we produce clean interpolated data in formats suitable for most modern ML-based trajectory forecasting dataloaders such as [45]. We do so by defining a 3D geographical fence around the airport of interest, as shown in Figure 2, filtering the position reports that fall inside it and within 2000 ft above ground level. We also extract relevant metadata from each position report, which we then interpolate and resample at 1-Hz. We produce per-hour,per-airport tabular files in CSV format containing the information shown in Table 1.

We open-source a toolkit for downloading and processing trajectory data from desired timeframes at github.com/AmeliaCMU/AmeliaSWIM.

Table 1 Fields with corresponding units and descriptions in the *Amelia-42* dataset.

Field	Units	Description	Field	Units	Description
Frame	#	Timestamp	Altitude	feet	Agent Altitude (Mean Sea Level)
ID	#	STDDS Agent ID	Range	km	Distance from airport datum
Speed	knots	Agent Speed	Bearing	rads	Bearing Angle w.r.t. North
Heading	degrees	Agent Heading	Type	int	Agent Type [0:A/C, 1:Veh, 2:Unk]
Lat	decimal degs	Latitude of the agent	x	km	Local X Cartesian Position
Lon	decimal degs	Longitude of the agent	y	km	Local Y Cartesian Position
Interp	boolean	Interpolated data point flag			

B. Map Data

We use OpenStreetMap (OSM) [46] and OSMNx [47] to create surface maps for the airports in *Amelia-42*. Raw OSM airport maps are dense routing graphs containing centerline information of the movement areas, pavement boundaries, and semantic information, e.g., taxiways, runways, hold-short lines, exit lines, aprons, etc. Node elements within the graph contain geographical coordinates (latitude, longitude) and local Cartesian coordinates, (x, y) , expressed w.r.t. an arbitrary origin.

We develop an automatic graph generation pipeline described in Appendix B.C that sanitizes raw OSM maps into compact vectorized semantic graphs, following [32]. The provided maps are stored as a collection of vectors representing the edges pertaining only to the centerline of movement areas $G = \{v_0, v_1, \dots, v_E\}$. Each vector contains information about the start and endpoint, both in terms of GPS coordinates and local Cartesian Coordinates; a categorical value representing the class of the zone the edge belongs to; and a numeric identifier, see Table 2 for a breakdown.

Table 2 Attributes for each of the edges in the vectorized graph.

Field	Contents	Description
Start	(latitude, longitude, y, x)	Starting coordinates for the graph edge. We include both GPS coordinates as well as Cartesian coordinates.
End	(latitude, longitude, y, x)	End coordinates for the graph edge.
Semantic ID	Integer	Map Zone Type: [1: hold-short line, 2: other, 3: runway, 4: taxiway]
ID	Integer	Unique Numeric Identifier

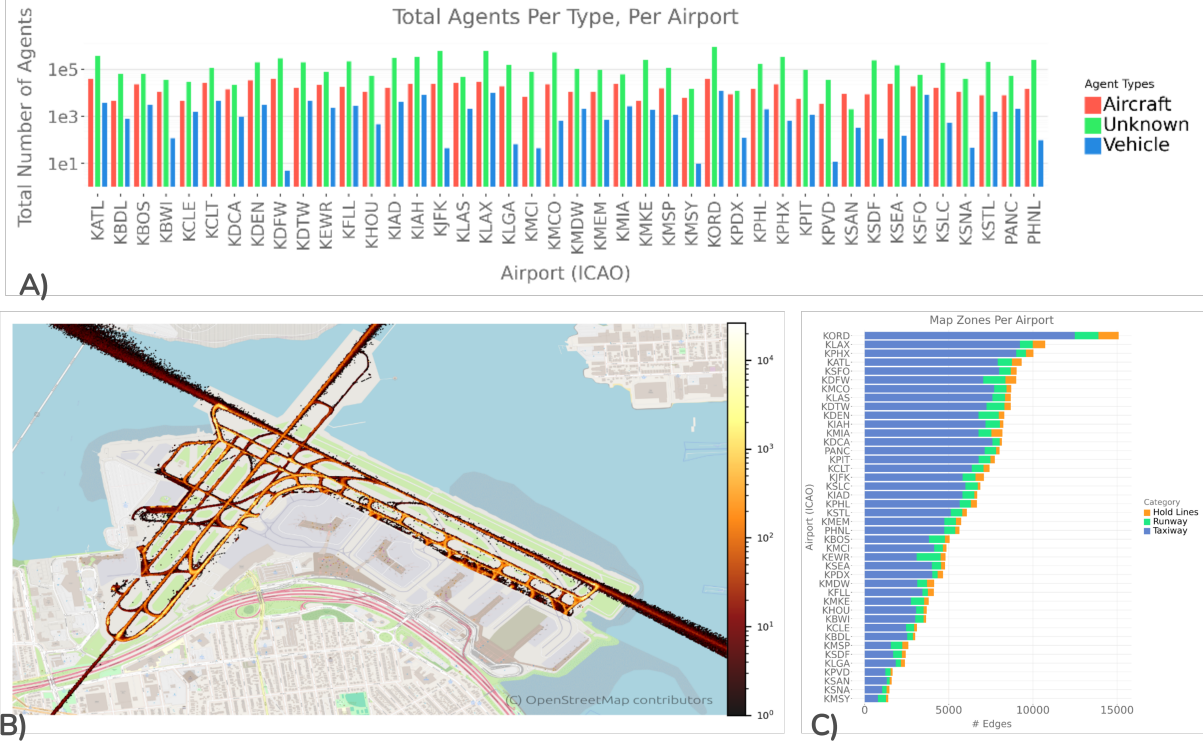


Fig. 3 Analysis of the Amelia42-Mini subset. A) Shows the total number of agents, per type (Aircraft, Unknown, Vehicle). B) Shows an airport’s heatmap, representing the activity frequency per region in the airport (darker, low frequency; brighter, high frequency). C) Shows the distribution of zone types (Taxiway, Runway, Hold-short Line) per airport’s map.

IV. Dataset Analysis

To facilitate usability and accessibility of our dataset, we release a 630-day subset of processed data as Amelia42-Mini at HuggingFace[†]. The subset covers 42 airports, randomly sampling 15 days per airport from the full dataset to capture diverse seasons and operational settings. In total, Amelia42-Mini contains ~8.43M unique agents, covering ~1.10B position reports, as well as processed maps for each airport.

Below, we provide a trajectory and map analysis of the subset and refer the reader to Appendix C for a more in-depth, per-airport breakdown.

[†] Access the Amelia42-Mini subset at: huggingface.co/datasets/AmeliaCMU/Amelia42-Mini

Trajectory Data Analysis. Figure 1 shows the total number of aircraft observed at each selected airport, identified by their International Civil Aviation Organization (ICAO) code. This highlights the variation in airport size and includes examples of diverse interaction scenarios. Figure 3.A) presents the agent type breakdown per airport. Overall, the *Amelia42-Mini* boasts over 708.88k aircraft, 90.14k vehicles, and 7.63M unknown agent types. As shown, the majority of the processed agents fall under the *unknown* category. It’s important to note that this is not a result of our data processing pipeline, but rather a limitation inherent to the SWIM STTDS service and infrastructure utilized for data collection. Nonetheless, even if removing the *unknown* agent types from our dataset, the scale and quality of the data are still substantial, and we believe that future work could explore re-labeling strategies to further enhance the quality of the data.

Figure 3.B) illustrates the spatial data coverage for the La Guardia Airport (*KLGA*), as a heatmap showing the activity frequency, bright spots represent concurred regions and capture critical section such as intersections and hold-lines; this showcases that our subset can capture operation hotspots relevant for behavior modeling.

Map Data Analysis. Figure 3.C) summarizes the distribution of zone types per airport map. Each airport is shown as a stacked barplot presenting the number of edges per category in its corresponding semantic graph, i.e., *Taxiway*, *Runway*, *Hold-short Line*. In all cases, the majority of the map information is comprised of taxiway edges, which represent the routes to and out of the runways, while critical regions like runways and hold lines are less predominant in each airport. The figure also shows that our map data has a diversity of map scales and densities. For instance, with airports like *KORD* and *KLAX* with over 10k edges, and others like *KMSY* with 1k edges.

V. A Trajectory Forecasting Benchmark

The *Amelia10-Bench* is a scenario benchmark for trajectory forecasting in crowded airport environments. The goal of trajectory forecasting is to predict the future scene given the previous observation, i.e., estimating the conditional probability distribution of the future scene, given the observations from the past time steps. For this task, we propose a scene representation that is long enough to capture long-horizon and diverse maneuvers in airspace.

A. Task Setup

Scenario Representation. We split the data into $T = 60$ seconds scenes to capture long-horizon interactions, where the first $H = 10$ seconds are the historical segment and the remaining $F = 50$ seconds are for prediction to encourage long-horizon and preemptive reasoning from minimal historical information. To split the data into a *train/val* and *test* sets, we use a *day*-based splitting strategy where 80% of each airport’s collected days are used for training/validation and the remaining 20%, for testing.

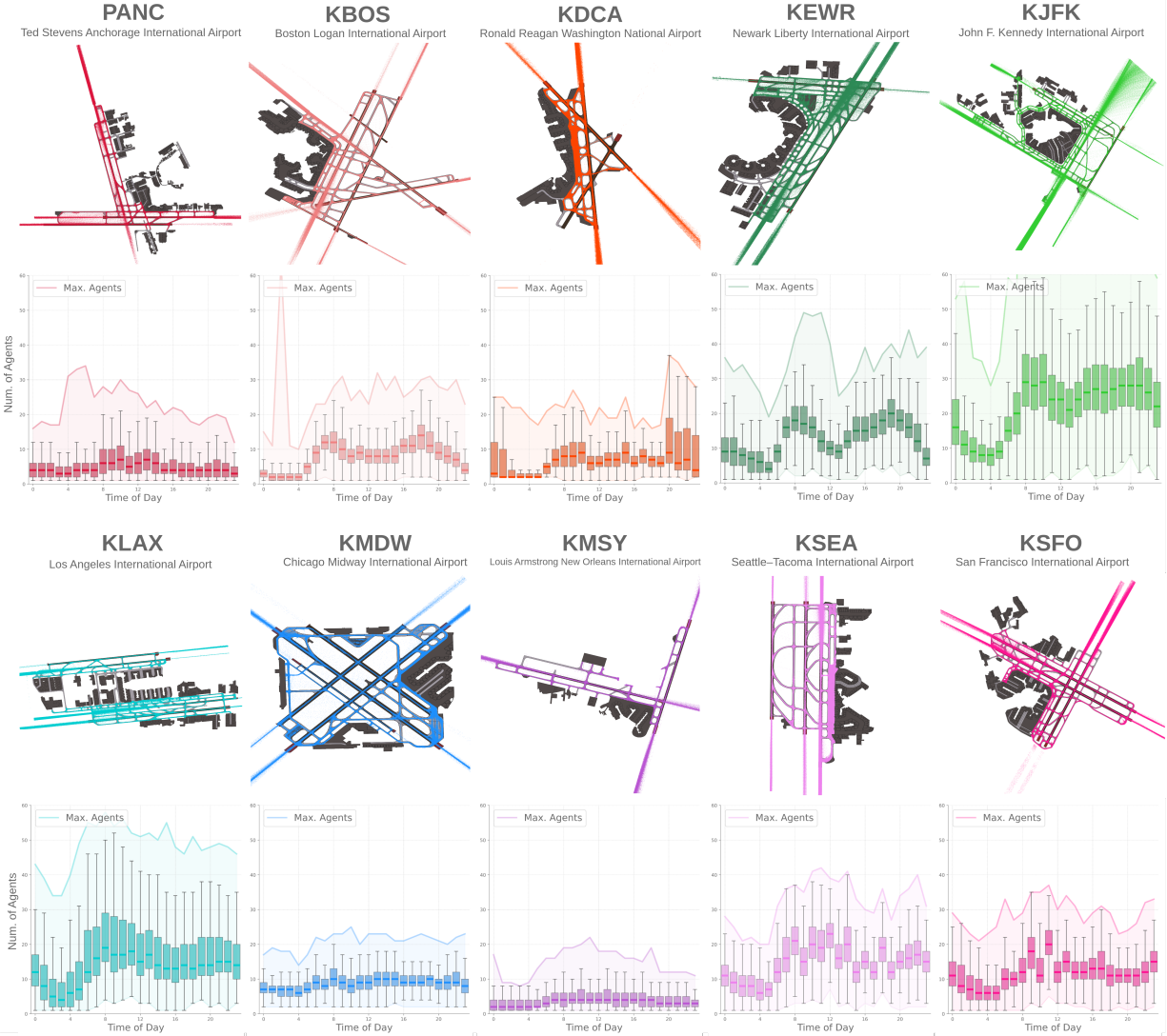


Fig. 4 Analysis of the Amelia10-Bench data. For each airport, we overlay a month’s worth of processed trajectories spanning beyond runway limits to capture landing and take-off rolls. We also show each airport’s crowdedness per hour of day.

Benchmark Data. For benchmarking, we limit to a 10-airport subset of the Amelia-42 spanning 292 days to keep the size of data under 50 GB so that the task is computationally accessible, while still providing more than 20M diverse scenarios. The tabular subset is accessible at HuggingFace and we release the tools to process the data into scenarios for trajectory forecasting[‡]

The airports are chosen to ensure diversity in map topologies and traffic density as depicted in Figure 4, but also based upon prior incident history [5]. We provide a comprehensive analysis showing the behavioral and environmental diversity of the data utilized for this study in Appendix D.

[‡]Access the Amelia10-Bench subset at: huggingface.co/datasets/AmeliaCMU/Amelia-10, and the scenario processing tool at: github.com/AmeliaCMU/AmeliaScenes

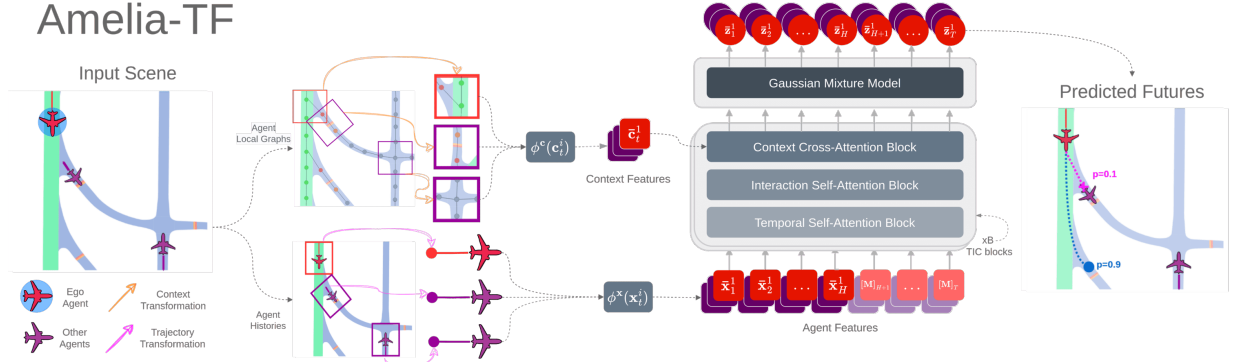


Fig. 5 An Overview of Amelia-TF.

The benchmark provides rich data that can support various experiments in airspace trajectory forecasting. As shown in Figure 4, each airport presents a large number of specific challenges, which form a unique domain. This benchmark can be used for in-domain training of specialized models, e.g., predicting a landing at the Seattle-Tacoma Airport after training on that setting. At the same time, this benchmark can also be used for cross-domain generalization to develop robust models that can handle uncertainty in unseen airports. We show both examples in Section V.B.

B. Experiment Family

For the purpose of our experiments for *in-domain* and *cross-domain* evaluation, we propose two main challenges. The first is `SingleAirport`, where we focus on assessing *in-domain* trajectory forecasting performance by training and testing our model’s performance one airport at a time. This setting, therefore, consists of 10 experiments, one per environment, and serves to encourage the development of specialized models.

The second challenge is `MultiAirport`, which consists of various experiments to assess *cross-domain* generalization of predictive models as we increasingly constrain the number of training environments. The sweep consists of 6 experiments: 10-Seen, 7-Seen, 4-Seen, 3-Seen, 2-Seen, and 1-Seen, each named according to the number of training (*seen*) airports[§]. This proposed challenge aims to focus on developing representation learning strategies that enable zero-shot generalization. Therefore, it aims to minimize the performance drop between *in-domain* and *cross-domain* and, in doing so, identify a practical compromise between training-set scale and cross-airport generalizability, ultimately bridging the gap between `SingleAirport` and `MultiAirport`. In Appendix D.C, we further detail the airport selection criteria for this challenge.

VI. A Trajectory Forecasting Baseline

To provide baseline results for the `Amelia10-Bench` benchmark, we introduce `Amelia-TF`, a trajectory forecasting model that aims to characterize *safety-relevant* airport surface movements. We build upon the intuitions from prominent

[§]The experiments with a greater number of *seen* airports are supersets of those with a smaller number.

state-of-the-art models to design a model capable of learning strong feature representations [35, 37], as well as automated methods for selecting relevant scenes and agents to characterize [48]. An overview of the model is shown in Figure 5, and briefly described below. Full algorithmic details on safety-critical scene representation and the model implementation are described in Section E.A and Appendix E.B, respectively.

A. Model Architecture

Scene Encoder. To encode the scene, we follow a transformer-based architecture that uses a factorized attention scheme for efficient computations as in [37, 49]. The model maintains a $K \times F \times D$ representation across all transformer layers while interleaving two types of self-attention layers: a *temporal* and an *interaction* one, as well as a *context* cross-attention layer as shown in Figure 5. Our scene encoder consists of multiple blocks combining these layers sequentially to obtain a richer representation (See Appendix E.B).

Trajectory Decoder. To model the distribution of possible futures for a scene, we adopt a Gaussian Mixture Model (GMM) as [35, 50], modeled as an MLP which takes the scene encoder’s final output features and produces and decodes F future timesteps over M modes as $(\mu, \Sigma, \rho)_{m,t}^i$ representing the mean, covariance and likelihood over a state for an agent, mode, and timestep.

Training Loss. We formulate the following loss function, $\mathcal{L} = \mathcal{L}^{nl} + \mathcal{L}^{ce}$, where \mathcal{L}^{nl} is a *regression* component which back-propagates the average negative log-likelihood between the predictions and ground truth, and \mathcal{L}^{ce} is a *classification* component which considers the cross-entropy between the model’s predicted confidences for each of the M prediction heads and the one-hot encoding of the predicted future with the smallest error.

B. Baseline Results on the Amelia10-Bench

We now study the performance of Amelia-TF on the Amelia10-Bench. We thus report short-horizon results in Table 3 and long-horizon results in Table 4. Each column shows the mADE/mFDE results for a given airport’s test set, and the last column shows the average across all airports. For reference, the first row shows SingleAirport results, and each of the remaining rows represents a MultiAirport experiment. In MultiAirport, the white and gray cells represent the seen (*in-domain*) and unseen (*cross-domain*) airports for the given experiment, respectively. We **bold** the best mADE/mFDE values across the experiment sweep and show in **green** the values that were lower than the results obtained in SingleAirport.

Short-Horizon Trajectory Forecasting Results. Our experiments show that generalization across unseen airports improves significantly as we increase the diversity and scale of seen environments. However, we also observe that our model generally exhibits strong performance even in more data-constrained experiments. We attribute this, in part, to

our scene representation strategy, which aims to abstract and prioritize scene information more effectively. Nonetheless, a gap between experiments across the sweep still remains. The results show that the 7-Seen experiment achieves the lowest average mADE/mFDE from the sweep of experiments, closing the gap to SingleAirport to +1.60%/-2.35%. Furthermore, results across all airports as well the results for KSEA, KDCA, PANC and KLAX as lower than those obtained in SingleAirport.

Table 3 We show Amelia10-Bench results for a prediction horizon of F=20.

Experiment	KMDW mADE / mFDE	KEWR mADE / mFDE	KBOS mADE / mFDE	KSFO mADE / mFDE	KSEA mADE / mFDE	KDCA mADE / mFDE	PANC mADE / mFDE	KLAX mADE / mFDE	KHSY mADE / mFDE	KJFK mADE / mFDE	Average mADE / mFDE
Single-Airport	3.30 / 6.12	6.61 / 12.92	5.58 / 10.90	5.06 / 9.82	9.76 / 18.35	4.74 / 9.22	10.11 / 20.87	11.36 / 20.63	2.73 / 5.12	4.58 / 9.52	6.38 / 12.35
10-Seen	3.88 / 7.70	7.87 / 15.80	6.87 / 14.34	6.09 / 12.64	9.03 / 18.35	4.84 / 9.55	8.24 / 16.75	8.80 / 16.73	3.22 / 6.25	4.56 / 9.64	6.34 (+0.70%) / 12.77 (-3.35%)
7-Seen	3.59 / 7.03	7.30 / 14.54	6.59 / 13.59	5.73 / 11.65	8.30 / 16.71	4.55 / 8.82	7.48 / 14.94	9.99 / 19.35	4.64 / 9.85	4.66 / 9.96	6.28 (+1.60%) / 12.64 (-2.35%)
4-Seen	3.52 / 6.74	7.26 / 14.33	6.31 / 12.68	5.66 / 11.33	9.79 / 20.42	5.99 / 12.28	9.22 / 19.14	10.70 / 21.16	4.18 / 9.05	4.80 / 10.27	6.74 (-5.32%) / 13.74 (-10.15%)
3-Seen	3.26 / 6.59	7.25 / 14.20	6.05 / 12.11	7.25 / 15.50	9.90 / 20.95	6.16 / 12.74	9.53 / 20.26	10.99 / 21.86	4.33 / 9.29	4.96 / 10.54	6.97 (-8.74%) / 14.40 (-14.29%)
2-Seen	3.31 / 6.23	6.92 / 13.45	8.17 / 17.63	7.49 / 17.18	10.57 / 22.86	6.04 / 12.47	10.61 / 23.00	12.78 / 26.34	4.49 / 9.64	5.21 / 11.15	7.56 (-15.56%) / 15.99 (-22.81%)
1-Seen	3.30 / 6.12	13.76 / 30.91	11.30 / 25.58	9.68 / 21.73	14.07 / 31.44	7.80 / 16.07	15.00 / 33.75	15.49 / 33.13	7.43 / 17.11	7.40 / 16.77	10.52 (-39.33%) / 23.26 (-46.92%)

Long-Horizon Trajectory Forecasting Results. Our experiments also show that generalization across unseen airports improves significantly as we increase the diversity and scale of seen environments. However, the gap between experiments is further exacerbated in contrast to short-horizon predictions. The results show that the All-Seen experiment achieves the lowest average mADE/mFDE from the full sweep of experiments, closing the gap to SingleAirport to -4.68%/-4.83%. Our model achieves better results for PANC, KLAX, KJFK than in SingleAirport.

Table 4 We show Amelia10-Bench results for a prediction horizon of F=50, reported in meters.

Experiment	KMDW mADE / mFDE	KEWR mADE / mFDE	KBOS mADE / mFDE	KSFO mADE / mFDE	KSEA mADE / mFDE	KDCA mADE / mFDE	PANC mADE / mFDE	KLAX mADE / mFDE	KHSY mADE / mFDE	KJFK mADE / mFDE	Average mADE / mFDE
Single-Airport	11.50 / 28.80	23.68 / 57.63	21.34 / 53.76	17.05 / 40.23	29.94 / 65.82	16.42 / 40.57	38.84 / 101.89	36.08 / 88.25	9.89 / 25.68	17.11 / 41.19	22.18 / 54.39
All-Seen	15.30 / 40.91	28.76 / 70.23	28.52 / 73.57	22.63 / 53.78	30.41 / 68.98	17.86 / 44.88	30.19 / 72.78	29.73 / 72.46	12.31 / 33.04	17.00 / 40.92	23.27 (-4.68%) / 57.16 (-4.83%)
7-Seen	14.35 / 38.62	26.83 / 66.12	27.57 / 71.84	20.81 / 50.01	28.29 / 64.69	16.40 / 41.25	27.40 / 66.74	34.60 / 85.90	19.87 / 54.56	17.71 / 42.84	23.38 (-5.12%) / 58.26 (-6.63%)
4-Seen	12.71 / 31.64	25.54 / 59.18	23.88 / 58.45	19.78 / 46.72	33.36 / 73.86	22.40 / 54.04	35.24 / 83.90	36.42 / 85.11	17.93 / 47.47	18.58 / 43.97	24.58 (-9.76%) / 58.43 (-6.92%)
3-Seen	12.46 / 31.81	25.15 / 57.29	23.20 / 56.48	28.33 / 67.40	35.70 / 81.02	24.32 / 59.55	38.85 / 92.94	39.02 / 91.96	19.53 / 51.52	19.37 / 47.06	26.59 (-16.57%) / 63.70 (-14.61%)
2-Seen	11.84 / 29.89	24.62 / 59.04	34.89 / 88.52	31.69 / 78.28	40.37 / 96.33	24.00 / 62.72	43.30 / 107.04	48.91 / 122.31	19.29 / 51.33	20.54 / 51.20	29.94 (-25.92%) / 74.67 (-27.15%)
1-Seen	11.50 / 28.80	56.14 / 140.59	48.16 / 124.34	40.54 / 103.97	54.24 / 130.67	28.90 / 73.87	61.62 / 156.56	63.20 / 164.52	30.59 / 80.23	29.51 / 73.97	42.44 (-47.73%) / 107.75 (-49.52%)

We present various scene examples with prediction results in Appendix E.C and further scenario analyses in Appendix E.D.

VII. Limitations & Future Work

While this work marks a significant advancement in facilitating large-scale open-source aviation research, it is not without its limitations. Here, we outline three interesting areas for future work in this field:

Managing Dataset Scale and Data Curation Amelia-42 logs over 2 years of position reports across 42 airports in the US National Airspace, the sheer scale of this data makes processing and curating a significant challenge. Within the scope of this project, we release random subsets of data in an attempt to provide diverse settings while introducing

minimal bias. However, future works could explore deriving different subsets from *Amelia-42* for specialized research lines; for instance, mining safety-critical incidents.

Tackling Generalizability and Long-Horizon Reasoning Challenges in Motion Forecasting. *Amelia-TF* was designed and introduced as a baseline to encourage further research in motion forecasting in aviation. We believe that crafting representation learning strategies that facilitate domain adaptation and generalization to previously unseen situations offers a promising path for future exploration. Additionally, we see aviation as an ideal field for enhancing and refining the long-horizon reasoning capabilities of predictive models, as long-horizon prediction could facilitate the preemptive identification and remediation of critical scenarios.

Downstream Applications of Motion Forecasting in Aviation. Predictive models for airport operations can be used for various tasks. For instance, *Amelia-TF* model can be combined with provably safe methods [18, 51] to provide data-driven collision risk assessment and decision-support systems to mitigate near misses and critical scenarios. Other avenues and applications could include leveraging models like *Amelia-TF* to improve taxi-out time predictions, departure metering, and time-of-arrival calculations for more efficient coordination of airport surface operations.

VIII. Conclusions

This work contributes *Amelia-42*, a large-scale dataset for airport surface movement, which comprises trajectory information and graph-based representations of the airport maps. We validate our dataset and data processing pipelines, providing statistical analyses, visualizations, and insights for 42 major U.S. airports. To the best of our knowledge, this is the **largest dataset of its kind in the public domain**, specifically geared toward training next-generation data-driven predictive models for airport surface operations. To encourage further research, we open-source both our code and data.

We also introduce *Amelia10-Bench*, a benchmark for trajectory forecasting in aviation, purposely designed to test the ability of architectures to leverage data for generalization to unseen settings. We contribute *Amelia-TF* as a baseline trajectory forecasting model, showcasing strong performance across various axes of analysis, exhibiting multi-future zero-shot generalization capabilities to previously unseen airports.

Funding Sources

This work was supported by Boeing (award #2022UIPA422). This work used Bridges-2 at Pittsburgh Supercomputing Center through allocation cis220039p from the Advanced Cyberinfrastructure Coordination Ecosystem: Services & Support (ACCESS) program, which is supported by National Science Foundation grants #2138259, #2138286, #2138307, #2137603, and #2138296. This work was also supported by the Korean Ministry of Trade, Industry, and Energy (MOTIE; grant #P0026022), and by the Korea Institute of Advancement of Technology (KIAT), through the International Cooperative R&D program (#P0019782): Embedded AI Based fully autonomous driving software and Maas technology development.

Acknowledgments

We thank Charles Erignac and Chad McFarland for their support and feedback throughout the project.

References

- [1] Daugherty, A., “‘We were very lucky’: Near-collisions spark new worries for air travel,” *POLITICO*, 2023.
- [2] Leussink, D., Kaneko, K., and Barrington, L., “Japan Airlines counts losses from wrecked Tokyo Plane,” *Reuters*, 2024.
- [3] Helmuth Rosales, M. G., K.K. Rebecca Lai, and Ismay, J., “What the Black Hawk Pilots Could See, Just Before the Crash,” *The New York Times*, 2025.
- [4] Ruberg, S., “1 Killed as Plane Owned by Mötley Crüe Singer Strikes Parked Jet,” *The New York Times*, 2025.
- [5] Ember, S., and Steel, E., “Airline Close Calls Happen Far More Often Than Previously Known,” *The New York Times*, 2023.
- [6] Krolik, A., “285 of 313 Air Traffic Control Facilities Are Understaffed,” *The New York Times*, 2025.
- [7] Association, I. A. T., “Air Passenger Market Analysis - December 2022,” Tech. rep., IATA, 2022.
- [8] Aratani, L., “TSA broke record on Sunday for number of passengers screened,” *The Washington Post*, 2023.
- [9] Degas, A., Islam, M. R., Hurter, C., Barua, S., Rahman, H., Poudel, M., Ruscio, D., Ahmed, M. U., Begum, S., Rahman, M. A., et al., “A survey on artificial intelligence (ai) and explainable ai in air traffic management: Current trends and development with future research trajectory,” *Applied Sciences*, Vol. 12, No. 3, 2022, p. 1295.
- [10] Sun, P., Kretzschmar, H., Dotiwalla, X., Chouard, A., Patnaik, V., Tsui, P., Guo, J., Zhou, Y., Chai, Y., Caine, B., et al., “Scalability in perception for autonomous driving: Waymo open dataset,” *Proceedings of the IEEE/CVF conference on computer vision and pattern recognition*, 2020, pp. 2446–2454.
- [11] Chang, M., Lambert, J., Sangkloy, P., Singh, J., Bak, S., Hartnett, A., Wang, D., Carr, P., Lucey, S., Ramanan, D., and Hays, J., “Argoverse: 3D Tracking and Forecasting With Rich Maps,” *IEEE Conference on Computer Vision and Pattern*

- Recognition, CVPR 2019, Long Beach, CA, USA, June 16-20, 2019*, Computer Vision Foundation / IEEE, 2019, pp. 8748–8757.
<https://doi.org/10.1109/CVPR.2019.00895>.
- [12] Caesar, H., Bankiti, V., Lang, A. H., Vora, S., Liong, V. E., Xu, Q., Krishnan, A., Pan, Y., Baldan, G., and Beijbom, O., “nuscnets: A multimodal dataset for autonomous driving,” *Proceedings of the IEEE/CVF conference on computer vision and pattern recognition*, 2020, pp. 11621–11631.
- [13] Rudenko, A., Palmieri, L., Herman, M., Kitani, K. M., Gavrilu, D. M., and Arras, K. O., “Human motion trajectory prediction: a survey,” *Int. J. Robotics Res.*, Vol. 39, No. 8, 2020. <https://doi.org/10.1177/0278364920917446>.
- [14] Pellegrini, S., Ess, A., Schindler, K., and Gool, L. V., “You’ll never walk alone: Modeling social behavior for multi-target tracking,” *IEEE 12th International Conference on Computer Vision, ICCV 2009, Kyoto, Japan, September 27 - October 4, 2009*, IEEE Computer Society, 2009, pp. 261–268. <https://doi.org/10.1109/ICCV.2009.5459260>.
- [15] Lerner, A., Chrysanthou, Y., and Lischinski, D., “Crowds by Example,” *Comput. Graph. Forum*, Vol. 26, No. 3, 2007, pp. 655–664. <https://doi.org/10.1111/j.1467-8659.2007.01089.x>.
- [16] Navarro, I., Patrikar, J., Dantas, J. P. A., Baijal, R., Higgins, I., Scherer, S., and Oh, J., “SoRTS: Learned Tree Search for Long Horizon Social Robot Navigation,” *IEEE Robotics and Automation Letters*, Vol. 9, No. 4, 2024, pp. 3759–3766. <https://doi.org/10.1109/LRA.2024.3370051>.
- [17] Patrikar, J., Dantas, J., Ghosh, S., Kapoor, P., Higgins, I., Aloor, J. J., Navarro, I., Sun, J., Stoler, B., Hamidi, M., et al., “Challenges in close-proximity safe and seamless operation of manned and unmanned aircraft in shared airspace,” *arXiv preprint arXiv:2211.06932*, 2022.
- [18] Muthali, A., Shen, H., Deglurkar, S., Lim, M. H., Roelofs, R., Faust, A., and Tomlin, C., “Multi-agent reachability calibration with conformal prediction,” *arXiv preprint arXiv:2304.00432*, 2023.
- [19] Sui, D., Chen, H., and Zhou, T., “A Conflict Resolution Strategy at a Taxiway Intersection by Combining a Monte Carlo Tree Search with Prior Knowledge,” *Aerospace*, Vol. 10, No. 11, 2023, p. 914.
- [20] Kong, Y., and Mahadevan, S., “Identifying Anomalous Behavior in Aircraft Landing Trajectory Using a Bayesian Autoencoder,” *Journal of Aerospace Information Systems*, 2023, pp. 1–9.
- [21] Memarzadeh, M., Matthews, B. L., and Weckler, D. I., “Anomaly Detection in Flight Operational Data Using Deep Learning,” *System-Wide Safety Technical Challenge 1 Close Out Event*, 2023.
- [22] Liu, Y., Hansen, M., Gupta, G., Malik, W., and Jung, Y., “Predictability impacts of airport surface automation,” *Transportation Research Part C: Emerging Technologies*, Vol. 44, 2014, pp. 128–145.
- [23] Lee, H., Malik, W., and Jung, Y. C., “Taxi-out time prediction for departures at Charlotte airport using machine learning techniques,” *16th AIAA Aviation Technology, Integration, and Operations Conference*, 2016, p. 3910.

- [24] Wang, F., Bi, J., Xie, D., and Zhao, X., “A data-driven prediction model for aircraft taxi time by considering time series about gate and real-time factors,” *Transportmetrica A: Transport Science*, Vol. 19, No. 3, 2023, p. 2071353.
- [25] Alsalous, O., and Hotle, S., “Deicing Facility Capacity and Delay Estimation Using ASDE-X Data: Chicago O’Hare Simulation Case Study,” *Transportation Research Record*, 2023, p. 03611981231185147.
- [26] Gui, X., Zhang, J., Peng, Z., and Yang, C., “Data-driven method for the prediction of estimated time of arrival,” *Transportation Research Record*, Vol. 2675, No. 12, 2021, pp. 1291–1305.
- [27] Li, M. Z., and Ryerson, M. S., “Reviewing the DATAS of aviation research data: Diversity, availability, tractability, applicability, and sources,” *Journal of Air Transport Management*, Vol. 75, 2019, pp. 111–130.
- [28] Zhang, X., Zhong, S., and Mahadevan, S., “Airport surface movement prediction and safety assessment with spatial–temporal graph convolutional neural network,” *Transportation research part C: emerging technologies*, Vol. 144, 2022, p. 103873.
- [29] Park, D. K., and Kim, J. K., “Influential factors to aircraft taxi time in airport,” *Journal of Air Transport Management*, Vol. 106, 2023, p. 102321.
- [30] Ranson, L., “FAA completes roll-out of ASDE-X anti-incursion surveillance,” *Flight International*, Vol. 180, No. 5313, 2011, pp. 15–15.
- [31] Patrikar, J., Moon, B., Oh, J., and Scherer, S., “Predicting like a pilot: Dataset and method to predict socially-aware aircraft trajectories in non-towered terminal airspace,” *2022 International Conference on Robotics and Automation (ICRA)*, IEEE, 2022, pp. 2525–2531.
- [32] Gao, J., Sun, C., Zhao, H., Shen, Y., Anguelov, D., Li, C., and Schmid, C., “Vectornet: Encoding hd maps and agent dynamics from vectorized representation,” *Proceedings of the IEEE/CVF Conference on Computer Vision and Pattern Recognition*, 2020, pp. 11525–11533.
- [33] Nayakanti, N., Al-Rfou, R., Zhou, A., Goel, K., Refaat, K. S., and Sapp, B., “Wayformer: Motion forecasting via simple & efficient attention networks,” *2023 IEEE International Conference on Robotics and Automation (ICRA)*, IEEE, 2023, pp. 2980–2987.
- [34] Cui, A., Casas, S., Wong, K., Suo, S., and Urtasun, R., “Gorela: Go relative for viewpoint-invariant motion forecasting,” *2023 IEEE International Conference on Robotics and Automation (ICRA)*, IEEE, 2023, pp. 7801–7807.
- [35] Shi, S., Jiang, L., Dai, D., and Schiele, B., “Motion transformer with global intention localization and local movement refinement,” *Advances in Neural Information Processing Systems*, Vol. 35, 2022, pp. 6531–6543.
- [36] Yuan, Y., Weng, X., Ou, Y., and Kitani, K. M., “Agentformer: Agent-aware transformers for socio-temporal multi-agent forecasting,” *Proceedings of the IEEE/CVF International Conference on Computer Vision*, 2021, pp. 9813–9823.

- [37] Ngiam, J., Vasudevan, V., Caine, B., Zhang, Z., Chiang, H.-T. L., Ling, J., Roelofs, R., Bewley, A., Liu, C., Venugopal, A., et al., “Scene transformer: A unified architecture for predicting future trajectories of multiple agents,” *International Conference on Learning Representations*, 2021, pp. 541–556.
- [38] Navarro, I., and Oh, J., “Social-PatteRNN: Socially-Aware Trajectory Prediction Guided by Motion Patterns,” *2022 IEEE/RSJ International Conference on Intelligent Robots and Systems (IROS)*, IEEE, 2022, pp. 9859–9864.
- [39] Alahi, A., Goel, K., Ramanathan, V., Robicquet, A., Fei-Fei, L., and Savarese, S., “Social lstm: Human trajectory prediction in crowded spaces,” *Proceedings of the IEEE conference on computer vision and pattern recognition*, 2016, pp. 961–971.
- [40] Zhao, D., and Oh, J., “Noticing motion patterns: A temporal cnn with a novel convolution operator for human trajectory prediction,” *IEEE Robotics and Automation Letters*, Vol. 6, No. 2, 2020, pp. 628–634.
- [41] Guo, D., Wu, E. Q., Wu, Y., Zhang, J., Law, R., and Lin, Y., “FlightBERT: Binary Encoding Representation for Flight Trajectory Prediction,” *IEEE Transactions on Intelligent Transportation Systems*, Vol. 24, No. 2, 2023, pp. 1828–1842. <https://doi.org/10.1109/TITS.2022.3219923>, URL <https://ieeexplore.ieee.org/document/9945661>, conference Name: IEEE Transactions on Intelligent Transportation Systems.
- [42] Guo, D., Zhang, Z., Yan, Z., Zhang, J., and Lin, Y., “FlightBERT++: A Non-autoregressive Multi-Horizon Flight Trajectory Prediction Framework,” *Proceedings of the AAAI Conference on Artificial Intelligence*, Vol. 38, No. 1, 2024, pp. 127–134. <https://doi.org/10.1609/aaai.v38i1.27763>, URL <https://ojs.aaai.org/index.php/AAAI/article/view/27763>, number: 1.
- [43] Zhang, Z., Guo, D., Zhou, S., Zhang, J., and Lin, Y., “Flight trajectory prediction enabled by time-frequency wavelet transform,” *Nature Communications*, Vol. 14, No. 1, 2023, p. 5258. <https://doi.org/10.1038/s41467-023-40903-9>, URL <https://www.nature.com/articles/s41467-023-40903-9>, publisher: Nature Publishing Group.
- [44] Yin, Y., Zhang, S., Zhang, Y., Zhang, Y., and Xiang, S., “Context-aware Aircraft Trajectory Prediction with Diffusion Models,” *2023 IEEE 26th International Conference on Intelligent Transportation Systems (ITSC)*, IEEE, 2023, pp. 5312–5317.
- [45] Ivanovic, B., Song, G., Gilitschenski, I., and Pavone, M., “trajdata: A unified interface to multiple human trajectory datasets,” *Advances in Neural Information Processing Systems*, Vol. 36, 2023, pp. 27582–27593.
- [46] Map, O. S., “Open street map,” *Online: https://www.openstreetmap.org. Search in*, 2014.
- [47] Boeing, G., “OSMnx: New methods for acquiring, constructing, analyzing, and visualizing complex street networks,” *Computers, Environment and Urban Systems*, Vol. 65, 2017, pp. 126–139.
- [48] Stoler, B., Navarro, I., Jana, M., Hwang, S., Francis, J., and Oh, J., “SafeShift: Safety-Informed Distribution Shifts for Robust Trajectory Prediction in Autonomous Driving,” *2024 IEEE Intelligent Vehicles Symposium (IV)*, 2024, pp. 1179–1186. <https://doi.org/10.1109/IV55156.2024.10588828>.
- [49] Ho, J., Kalchbrenner, N., Weissenborn, D., and Salimans, T., “Axial attention in multidimensional transformers,” *arXiv preprint arXiv:1912.12180*, 2019.

- [50] Chai, Y., Sapp, B., Bansal, M., and Anguelov, D., “Multipath: Multiple probabilistic anchor trajectory hypotheses for behavior prediction,” *arXiv preprint arXiv:1910.05449*, 2019.
- [51] Nakamura, K., and Bansal, S., “Online update of safety assurances using confidence-based predictions,” *2023 IEEE International Conference on Robotics and Automation (ICRA)*, IEEE, 2023, pp. 12765–12771.
- [52] Robb, J., “System wide information management (SWIM): program overview and status update,” *2014 Integrated Communications, Navigation and Surveillance Conference (ICNS) Conference Proceedings*, IEEE, 2014, pp. 1–15.
- [53] Vinoski, S., “Advanced message queuing protocol,” *IEEE Internet Computing*, Vol. 10, No. 6, 2006, pp. 87–89.
- [54] Glasmacher, C., Krajewski, R., and Eckstein, L., “An automated analysis framework for trajectory datasets,” *arXiv preprint arXiv:2202.07438*, 2022.
- [55] Melnychuk, V., Frauen, D., and Feuerriegel, S., “Causal transformer for estimating counterfactual outcomes,” *International Conference on Machine Learning*, PMLR, 2022, pp. 15293–15329.
- [56] Vaswani, A., Shazeer, N., Parmar, N., Uszkoreit, J., Jones, L., Gomez, A. N., Kaiser, Ł., and Polosukhin, I., “Attention is all you need,” *Advances in neural information processing systems*, Vol. 30, 2017.

Supplementary Material

A. Amelia Framework Supplementary

The Amelia framework shown in Figure 6 consists of a toolkit utilized for (1) collecting, visualizing, analyzing, and processing airport trajectory and map data, and (2) developing, training, and evaluating motion forecasting algorithms. We open-source all of these tools as a set of six GitHub repositories to facilitate data-driven research in the aviation domain at github.com/orgs/AmeliaCMU.

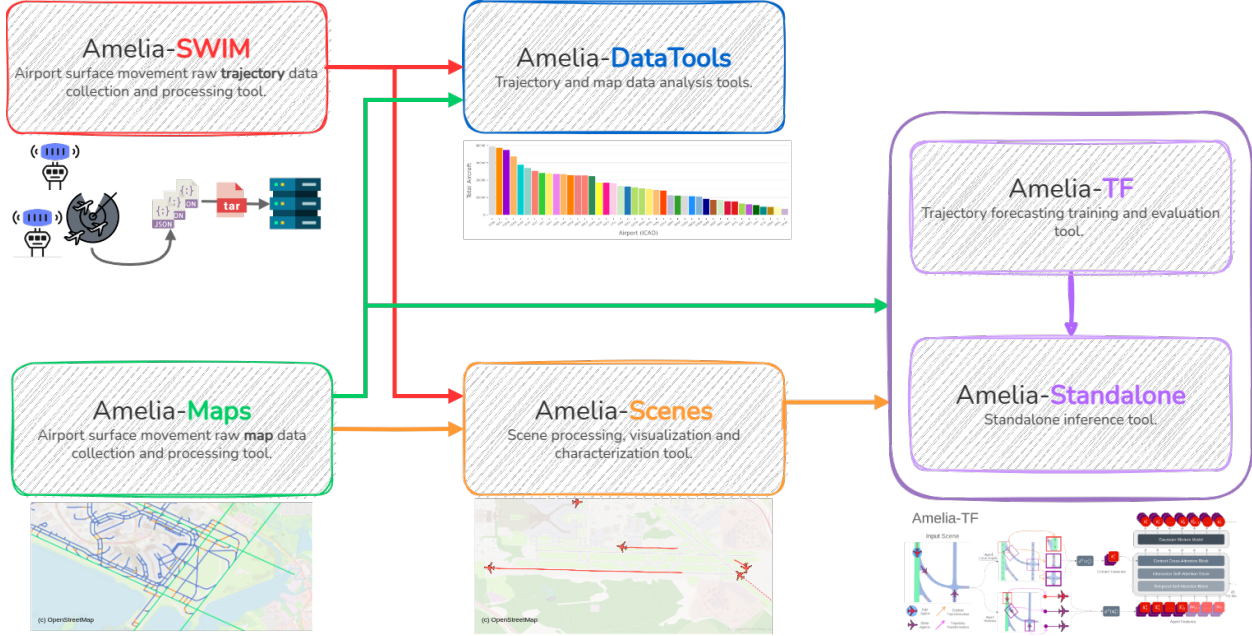


Fig. 6 Overview of the Amelia Framework.

Below, we provide a brief description of each of these repositories. Further sections in this supplementary provide more details about (1) data collection and processing (Appendix B); (2) in-depth analysis of our subsets Amelia42-Mini (Appendix C) and Amelia10-Bench (Appendix D); and (3) model design and additional experiments (Appendix E).

A. Amelia-SWIM

This tool provides scripts to **download** the raw trajectory data described in Section III.A, and to **process** the data into tabular form with the attributes described in Table 1. It also provides instructions on how to modify airport geo-fences. This enables custom regions to be processed in the vicinity of the airport.

The tool and usage instructions are available at: github.com/AmeliaCMU/AmeliaSWIM.

B. Amelia-Maps

This tool provides scripts to **process** the raw OpenStreetMap (OSM) [46] into the vectorized representation utilized in our work, and to visualize the process step-by-step. It also provides a script to obtain the OSM background maps utilized for visualization generation in this paper.

The tool and usage instructions are available at: github.com/AmeliaCMU/AmeliaMaps.

C. Amelia-DataTools

We offer scripts for analyzing and visualizing map and trajectory data. These scripts include tools for assessing agent counts at each airport (Figure 1, Figure 3), profiling motion (Figure 16, visualizing trajectory data over a corresponding map (Figure 2), dataset summaries (Table 6, Table 5, Table 7), and more.

The tool and usage instructions are available at: github.com/AmeliaCMU/AmeliaDataTools.

D. Amelia-Scenes

This tool is used for extracting scenes from the tabular data. Here scene is defined as a window of time in which interactions are analyzed. Our scene extraction is easily configurable to obtain different types of scenes in terms of the number of agents of interest, scene length, and granularity. It also provides filtering options to remove scenes with vehicles or unknown agents, if desired. We also provide scene characterization tools to analyze scene complexity w.r.t. individual agent kinematic profiles, as well as the level of agent-to-agent interactivity and crowdedness. Finally, we provide scripts with various strategies to split the data into `train/val/test` sets.

Scene examples are shown in Figure 1, Figure 19 and Figure 17.

The tool and usage instructions are available at: github.com/AmeliaCMU/AmeliaScenes.

E. Amelia-TF

We provide a framework for training and evaluating trajectory forecasting models that uses Hydra + Pytorch Lightning. This framework enables easy integration and implementation of existing and new models. We also release a standalone inference tool for visualizing model predictions.

The model architecture, configuration files, training/evaluation tools, and usage instructions are available at: github.com/AmeliaCMU/AmeliaTF.

F. Amelia-Inference

This tool is intended to be a standalone version of Amelia-TF, used only for inference purposes without the training/evaluation and prototyping overhead code from the latter repo.

The tools and usage instructions are available at: github.com/AmeliaCMU/AmeliaInference.

B. Amelia-42 Supplementary

Here, we describe in more detail the collection and processing steps we followed to create the Amelia-42 dataset.

A. Collecting the Raw Trajectory Data through SWIM

Amelia-42 leverages the FAA's System Wide Information Management (SWIM) Program [52], a repository of aviation data spanning the National Airspace System (NAS). Specifically, we utilize the SWIM Terminal Data Distribution System (STDDS), which aggregates terminal data from various sources like the Airport Surface Detection Equipment – Model X (ADSE-X) and the Airport Surface Surveillance Capability (ASSC) into easily accessible information. Position reports for zones covered by STDDS are made available as Surface Movement Events, streamed as a subscription via the NAS Enterprise Messaging Service (NEMS). These events are structured in an XML-like format, as shown in the example in Listing 1.

STDDS data is only available for airports that are covered by a Terminal Radar Approach Control (TRACON) facility. As a result, the raw dataset is a collection of Surface Movement Events covering TRACONs within the NAS since December 1st, 2022 (Unix Time Stamp: 1669944602). The Amelia-42 dataset continues to stream and archive these position reports on an ongoing basis.

Our recording scripts use two sets of 4 concurrent Advanced Message Queuing Protocol [53] connections for redundancy. Each connection records data for one hour and then closes the connection to offload the data to storage as a compressed newline JSON. The format of the files follows the structure: ALL_<#connection>_<UnixTimeStamp>.njson.gz. Every hour, the first set starts recording on the hour, and the next one starts 30 minutes later. Thus, at any given point, eight connections are active. Each connection deals with a manageable chunk of data to reduce onboard RAM usage and guard against data corruption. The scripts launch afresh automatically every 30 minutes, providing redundancy against server downtime and networking snags.

```
{ "properties": { "blockAtFAA": "false", "msgType": "ML", "sendTo": "all", "
  solace_routing_dest_name": "SMES/all/false/ML/KBOS/A90", "globalID": "1453771078",
  "msgSeqID": "157693832", "tracon": "A90", "timeline": "1736145001439 1736145001519
  1736145001519", "version": "4.0", "airport": "KBOS", "timestamp": "2025-01-06T06:30
  :01.439Z"}, "body": "<?xml version='1.0' encoding='UTF-8' standalone='yes'><
  ns2:asdexMsg xmlns:ns2='urn:us:gov:dot:faa:atm:terminal:entities:v4-0:smes:
  surfacemovementevent'><airport>KBOS</airport><mLatReport full='true'><report><
  basicReport><time>2025-01-06T06:30:01.250Z</time><track>3328</track><position><x>24
  8</x><y>79</y><lat>42.36647</lat><lon>-71.01542</lon></position><velocity><x>0.0</x
  ><y>0.0</y></velocity></basicReport><acAddress>A70F11</acAddress><height>-256.25</
  height></report><descriptor><crt>0</crt><rab>0</rab><spi>0</spi><gbs>1</gbs><tot>
  undetermined</tot><type>1</type></descriptor><status><cnf>confirmed</cnf><dou>1</
```

```

dou></status><extent><u>0</u><x>0</x><gm>0</gm><df>17</df><xxcovar>2.20000004768371
6</xxcovar><yycovar>3.9000000953674316</yycovar><zzcovar>100.0</zzcovar><xcovar>-5
.0</xcovar></extent><cachedData><mode3ACode>2000</mode3ACode><acAddress>A70F11</
acAddress></cachedData></mlatReport><mlatReport full=\ "false\ "><report><basicReport
><time>2025-01-06T06:30:01.289Z</time><track>3423</track><position><x>-277</x><y>-4
52</y><lat>42.3617</lat><lon>-71.02181</lon></position></basicReport><mode3ACode><
code>7160</code><g>0</g></mode3ACode></report><descriptor><crt>0</crt></descriptor
><extent><df>5</df><xxcovar>2.799999952316284</xxcovar></extent><enhancedData><
eramGufi>KT08053200</eramGufi></enhancedData></mlatReport></ns2:asdexMsg>"}
```

Listing 1 Sample of Surface Movement Event messages which are aggregated to form the raw dataset.

B. Geofence Creation

Before pre-processing the trajectory data into clean, tabular data suitable for motion forecasting, we need to define a region of interest representing the **surface movement areas** described in Section III. To do so, we define a 2D geographical fence around the airport of interest and then filter the position reports that fall inside it and within 2000ft above ground level. A few examples of GeoFences resulting from this process are shown in Figure 7.

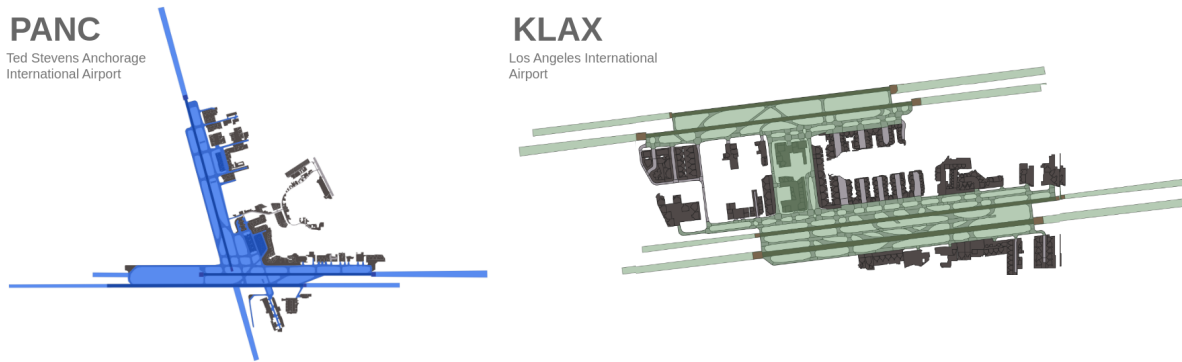


Fig. 7 Examples of geofences used for determining a region of interest to collect position reports within the airports' movement areas.

C. Automated Graph Generation

To obtain a more compact representation of the map, we apply a series of automated steps to only maintain elements of interest. We begin by filtering the graph such that only edges and nodes pertaining to centerlines of movement areas are maintained. These are then classified into the following semantic classes: runway, taxiway, and hold-lines, which indicate the exit boundary of runway-protected areas (Figure 8.b). We then extend runway endpoints by a nautical mile to encompass landing and take-off procedures (Figure 8.c). Lastly, we super-sample the runway centerlines to obtain a

finer runway representation (Figure 8.d).

Finally, following [32], we encode the graph in a vectorized manner (Figure 8.e), where an edge i is described as a vector, $v_i = [d_i^s, d_i^e, a_i]$, with $d_i^s \in \mathbb{R}^{1 \times 4}$ and $d_i^e \in \mathbb{R}^{1 \times 4}$ being the start and end nodes containing the geographical and relative coordinates, and $a_i \in \mathbb{N}^{1 \times 3}$ a one-hot encoded vector indicating one of semantic classes.

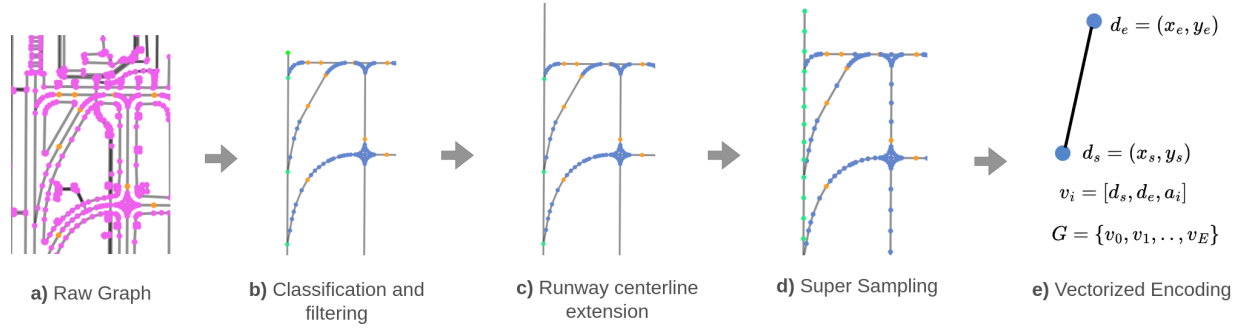


Fig. 8 Overview of our automated map processing pipeline, which converts raw maps from OpenStreetMap into compact, easy-to-use semantic airport graphs.

C. Amelia42-Mini Supplementary

Here, we provide additional analyses for the processed Amelia42-Mini subset.

A. Dataset Analysis

In Figure 9 we show the selected per-airport timeframes for the Amelia42-Mini subset. On the horizontal axis, we show the time span of the full Amelia-42 dataset as of May 22nd, 2025. To obtain the Amelia42-Mini subset, and reduce selection biases, we randomly select a starting point (left-most point in each airport's interval) across the timeline for each airport, and process the data for 15 subsequent days from the starting point (right-most point in the interval). Therefore, we show each airport's sample interval in the figure and the airport's ICAO code on the left. The legend includes the specific timeframes as a range YYYY-MM-DD - YYYY-MM-DD reported in the GMT-4 timezone.

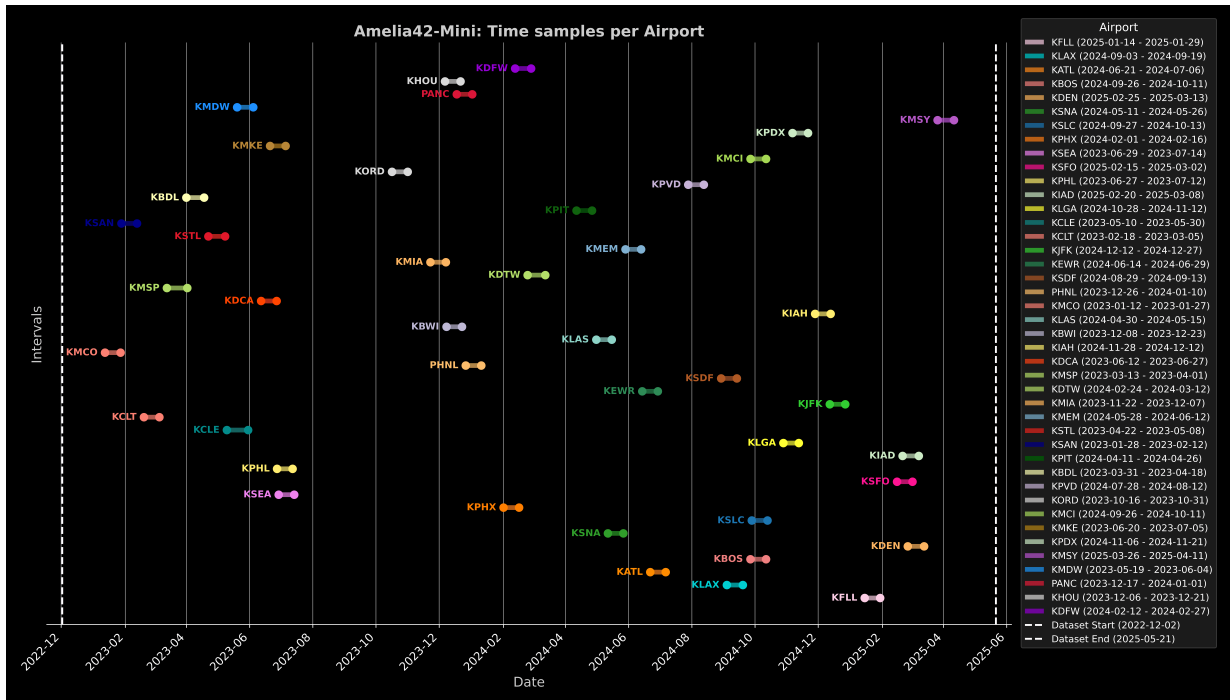


Fig. 9 Selected per-airport timeframes for the Amelia42-Mini subset.

Table 5 provides a quantitative summary of each airport’s traffic information for the Amelia42-Mini subset. It includes the *total* and *per-category* number of unique agents and unique data points. Like Figure 3, we include for reference the timespan for the sample we computed the counts, following the format YYYY-MM-DD HH:MM - YYYY-MM-DD HH:MM also reported in GMT-4 time. For each column, we color the cells to indicate relative scale w.r.t. maximum value in the column.

Table 5 Quantitative summaries for the Amelia42-Mini subset.

Airport	Timespan	Total		Aircraft		Vehicle		Unknown	
		Num. Agents	Num. Data Points	Num. Agents	Num. Data Points	Num. Agents	Num. Data Points	Num. Agents	Num. Data Points
KATL	2024-06-21 19:04 - 2024-07-06 18:04	410.11K	37.89M	38.67K	16.02M	3.77K	2.06M	367.61K	19.78M
KBDL	2023-03-31 20:51 - 2023-04-18 00:51	68.60K	6.02M	4.38K	1.20M	801	328.68K	63.42K	4.49M
KBOS	2024-09-26 12:11 - 2024-10-11 14:11	87.44K	21.11M	22.69K	10.61M	2.99K	2.63M	61.76K	7.86M
KBWI	2023-12-08 02:04 - 2023-12-23 01:04	45.36K	8.08M	11.22K	4.16M	118	50.51K	34.02K	3.87M
KCLE	2023-05-10 00:59 - 2023-05-30 12:59	35.88K	4.39M	4.52K	1.49M	1.52K	1.41M	29.85K	1.48M
KCLT	2023-02-18 21:58 - 2023-03-05 20:58	144.91K	28.77M	25.32K	13.01M	4.41K	2.86M	115.17K	12.90M
KDCA	2023-06-12 01:33 - 2023-06-27 00:33	37.15K	10.04M	13.97K	4.68M	930	952.03K	22.24K	4.40M
KDEN	2025-02-25 11:48 - 2025-03-13 05:48	229.60K	20.24M	33.63K	12.05M	3.17K	1.82M	192.80K	6.38M
KDFW	2024-02-12 09:33 - 2024-02-27 18:33	320.53K	88.77M	37.45K	23.40M	5	2.11K	283.07K	65.36M
KDTW	2024-02-24 10:25 - 2024-03-12 11:25	212.34K	28.69M	15.78K	7.57M	4.43K	2.55M	192.13K	18.56M
KEWR	2024-06-14 01:35 - 2024-06-29 03:35	101.42K	21.16M	22.28K	13.37M	2.25K	1.43M	76.88K	6.36M
KFLL	2025-01-14 20:48 - 2025-01-29 19:48	235.95K	26.42M	18.20K	10.19M	2.83K	1.92M	214.91K	14.30M
KHOU	2023-12-06 15:20 - 2023-12-21 14:20	64.90K	9.80M	10.89K	3.23M	461	293.23K	53.55K	6.29M
KIAD	2025-02-20 11:06 - 2025-03-08 03:06	327.11K	36.01M	16.63K	7.72M	4.16K	1.45M	306.32K	26.83M
KIAH	2024-11-28 00:45 - 2024-12-12 23:45	363.85K	61.22M	23.87K	13.50M	8.05K	3.87M	331.90K	43.79M
KJFK	2024-12-12 04:13 - 2024-12-27 03:13	615.27K	35.24M	24.11K	14.19M	44	20.53K	591.11K	21.03M
KLAS	2024-04-30 17:31 - 2024-05-15 16:31	76.76K	15.00M	26.98K	10.16M	2.05K	809.72K	47.73K	4.03M
KLAX	2024-09-03 18:42 - 2024-09-19 04:42	643.28K	49.02M	28.81K	10.90M	9.72K	2.42M	604.72K	35.69M
KLGA	2024-10-28 08:09 - 2024-11-12 07:09	171.71K	15.90M	18.46K	7.09M	65	21.94K	153.17K	8.79M
KMCI	2024-09-26 15:35 - 2024-10-11 14:35	80.81K	31.22M	6.46K	1.75M	44	37.21K	74.30K	29.43M
KMCO	2023-01-12 08:20 - 2023-01-27 08:20	541.20K	53.29M	22.68K	13.70M	644	277.79K	517.85K	39.29M
KMDW	2023-05-19 21:24 - 2023-06-04 11:24	118.06K	11.82M	10.70K	2.88M	2.14K	1.15M	105.22K	7.78M
KMEM	2024-05-28 22:40 - 2024-06-12 23:40	105.73K	16.89M	10.51K	4.44M	730	414.54K	94.49K	12.04M
KMIA	2023-11-22 12:56 - 2023-12-07 11:56	85.64K	15.15M	23.47K	10.71M	2.68K	894.51K	59.48K	3.54M
KMKE	2023-06-20 17:40 - 2023-07-05 16:40	261.35K	34.62M	4.46K	1.54M	1.86K	1.42M	255.03K	31.65M
KMSP	2023-03-13 02:34 - 2023-04-01 18:34	125.92K	18.23M	15.36K	6.70M	1.18K	784.28K	109.38K	10.75M
KMSY	2025-03-26 06:53 - 2025-04-11 01:53	20.93K	3.28M	5.99K	1.47M	10	10.39K	14.94K	1.80M
KORD	2023-10-16 11:52 - 2023-10-31 15:52	910.66K	72.77M	39.53K	22.57M	12.02K	11.66M	858.39K	38.00M
KPDX	2024-11-06 04:59 - 2024-11-21 03:59	20.47K	3.72M	8.52K	2.67M	119	37.90K	11.83K	1.02M
KPHL	2023-06-27 11:46 - 2023-07-12 10:46	186.58K	46.32M	14.88K	8.56M	1.97K	2.36M	169.73K	35.41M
KPHX	2024-02-01 04:06 - 2024-02-16 03:06	347.51K	41.46M	22.91K	9.88M	625	553.10K	323.98K	31.02M
KPIT	2024-04-11 15:42 - 2024-04-26 14:42	99.15K	22.37M	5.51K	2.04M	1.17K	816.24K	92.47K	19.51M
KPVD	2024-07-28 11:34 - 2024-08-12 13:34	37.58K	3.49M	3.33K	1.32M	12	6.72K	34.24K	2.16M
KSAN	2023-01-28 03:49 - 2023-02-12 05:49	11.47K	3.62M	9.19K	3.16M	317	112.98K	1.96K	351.27K
KSDF	2024-08-29 06:01 - 2024-09-13 10:01	241.46K	26.86M	8.57K	3.14M	113	106.41K	232.77K	23.61M
KSEA	2023-06-29 01:01 - 2023-07-14 00:01	167.14K	17.14M	23.57K	11.62M	146	149.44K	143.42K	5.37M
KSFO	2025-02-15 02:09 - 2025-03-02 01:09	85.55K	13.21M	18.42K	7.59M	8.40K	3.10M	58.73K	2.52M
KSLC	2024-09-27 21:00 - 2024-10-13 00:00	203.57K	37.34M	16.26K	6.18M	524	125.68K	186.76K	31.03M
KSMA	2024-05-11 21:46 - 2024-05-26 20:46	49.37K	5.66M	11.02K	4.66M	45	19.84K	38.31K	976.05K
KSTL	2023-04-22 04:14 - 2023-05-08 07:14	211.96K	72.38M	7.70K	2.89M	1.52K	1.54M	202.73K	67.95M
PANC	2023-12-17 23:41 - 2024-01-01 22:41	61.93K	8.65M	7.80K	2.71M	2.03K	1.47M	52.10K	4.47M
PHIL	2023-12-26 16:34 - 2024-01-10 15:34	265.90K	19.40M	14.17K	5.17M	96	60.60K	251.63K	14.17M
Total		8.43M	1.10B	708.88K	321.87M	90.14K	54.01M	7.63M	726.04M

In Figure 10 through 13, we present the per-timestep motion profiles of aircraft across all airports in the subset. From left to right, the plots display average speed, average acceleration, and heading change, with each row representing a different airport. These profiles reveal ample variability in speed and heading values, capturing the range of aircraft behaviors such as taxiing, take-off, landing, and vacating, as well as behavioral diversity resulting from topological variability.

The acceleration profiles feature a thin, elongated bin at 0m/s^2 , which corresponds, for instance, to stationary aircraft awaiting clearance or gate assignment, or agents moving at constant speed. Meanwhile, the higher acceleration and deceleration values align with aircraft during take-off and landing. Despite differences between airports, the trends in speed, acceleration, and heading change remain consistent, suggesting that *Amelia42-Mini* successfully captures representative and realistic ground operation behaviors.

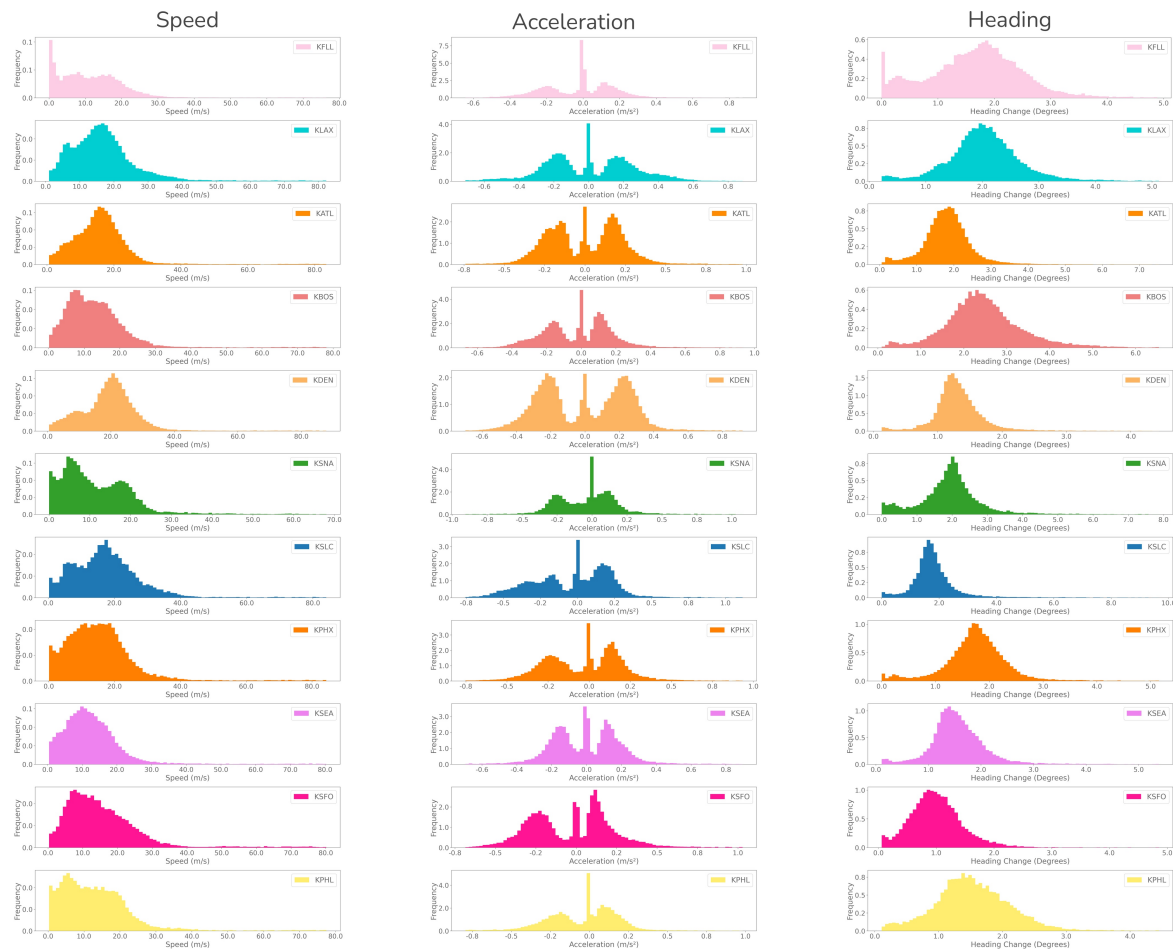


Fig. 10 Per-airport motion profiles. We show the per-timestep distribution over the aircraft’s speed, acceleration and heading. From top to bottom, we show the motion profiles for: KFL, KLAX, KATL, KBOS, KDEN, KSNA, KSLC, KPHX, KSEA, KSFO, KPHL.

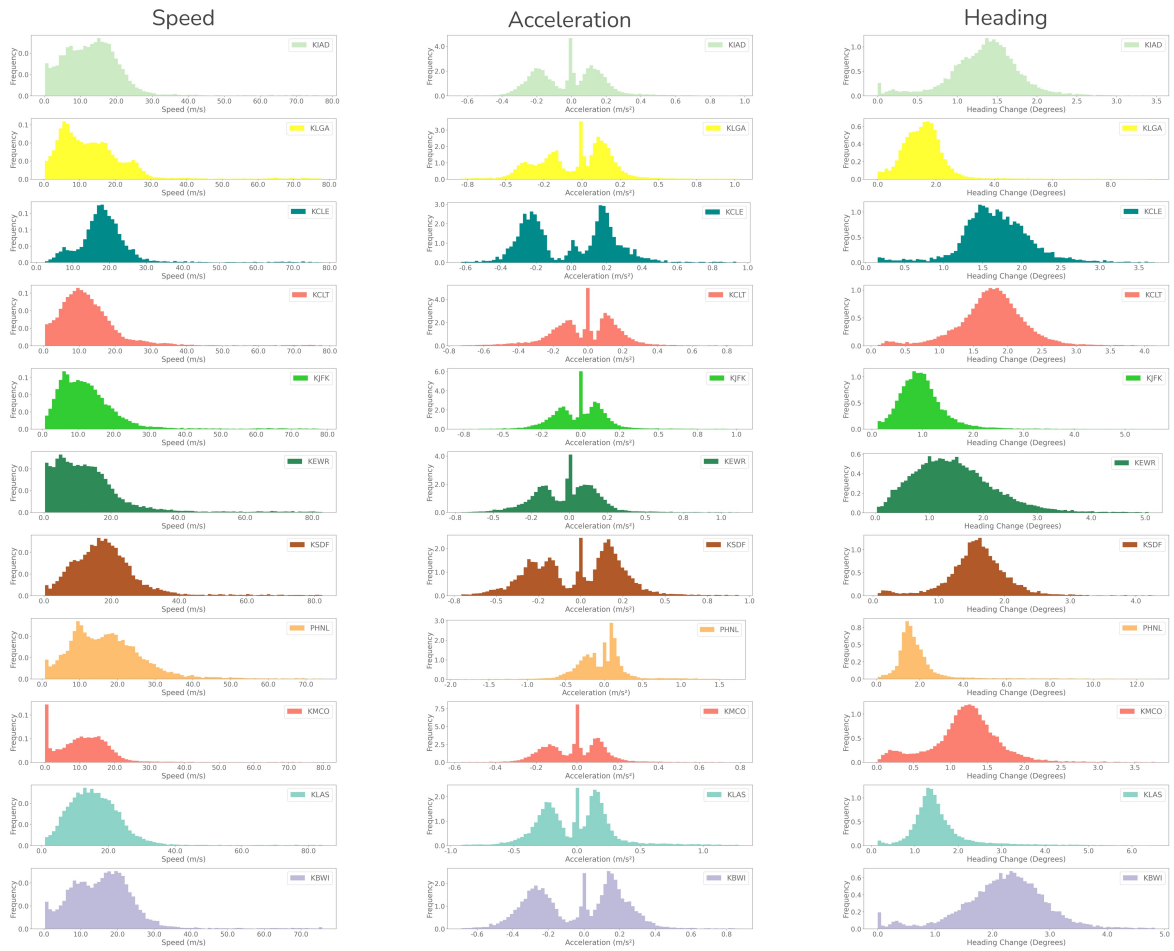


Fig. 11 Per-airport motion profiles. We show the per-timestep distribution over the aircraft’s speed, acceleration and heading. From top to bottom, we show the motion profiles for: KIAD, KLGA, KCLE, KCLT, KJFK, KEWR, KSDF, PHLN, KMCO, KLAS, KBWI.

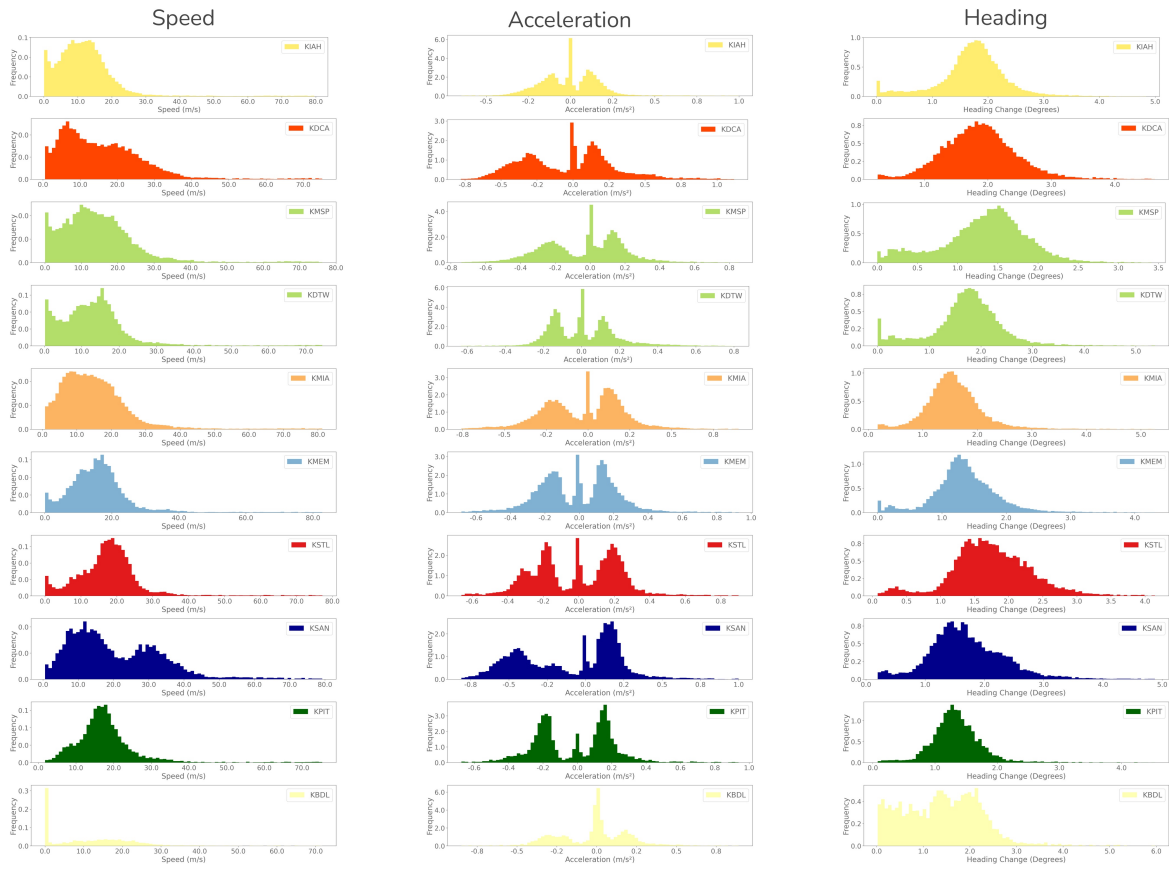


Fig. 12 Per-airport motion profiles. We show the per-timestep distribution over the aircraft's speed, acceleration and heading. From top to bottom, we show the motion profiles for: KIAH, KDCA, KMSP, KDTW, KMIA, KMEM, KSTL, KSAN, KPIT, KBDL.

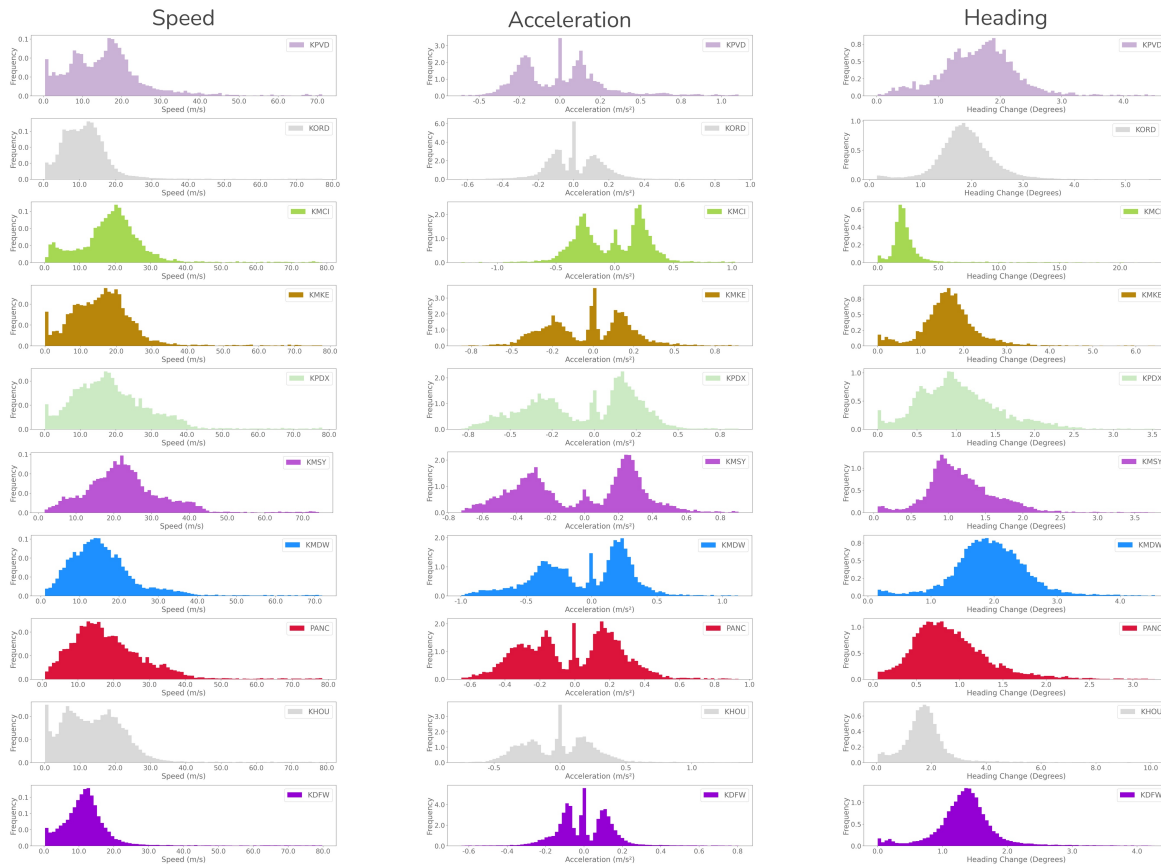
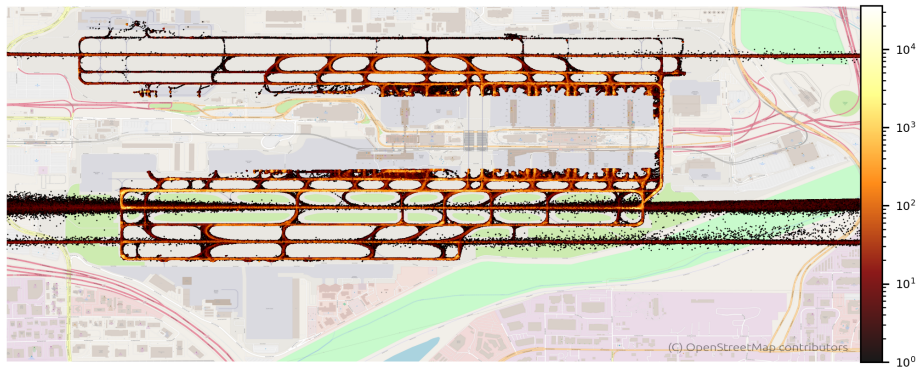


Fig. 13 Per-airport motion profiles. We show the per-timestep distribution over the aircraft's speed, acceleration and heading. From top to bottom, we show the motion profiles for: KPVD, KORD, KMCI, KMKE, KPDX, KMSY, KMDW, PANC, KHOU, KDFW.

KPHL



KPHX



KPIT

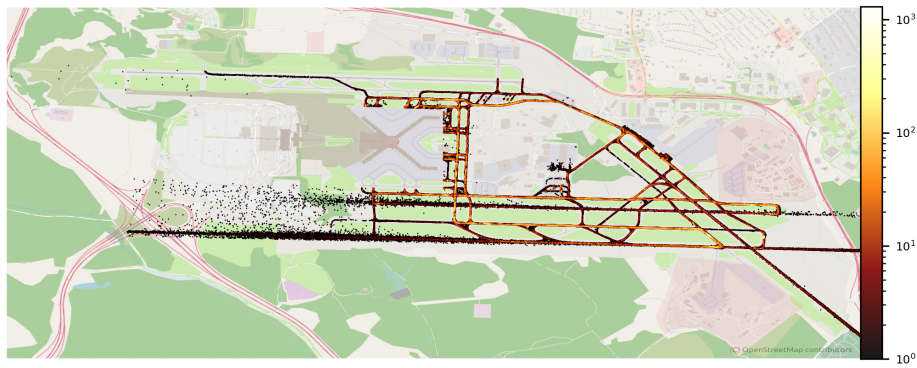
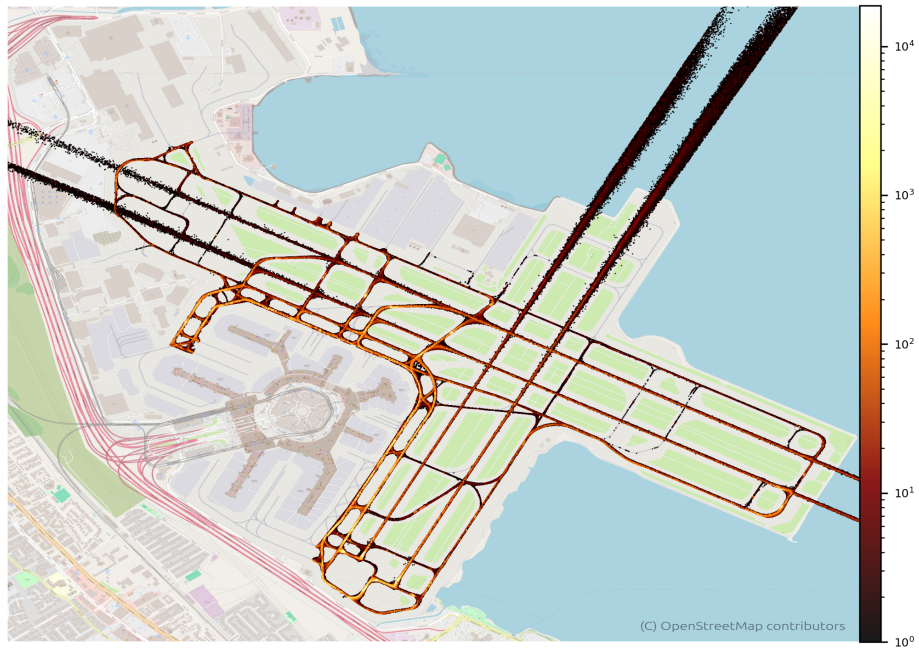


Fig. 14 Heatmap showing activity frequency for regions for airports KPHL, KPHX and KPIT

KSAN



KSFO



KSTL



Fig. 15 Heatmap showing activity frequency for regions for airports KSAN, KSFO and KSTL

D. Amelia10-Bench Supplementary

Amelia10-Bench is meant to provide a diverse set of settings and interactions for benchmarking trajectory forecasting performance. This section provides an analysis of the selected airports to support this objective.

A. Trajectory Data Analysis.

Table 6 provides a quantitative summary of each airport’s traffic information, including the *total* and *per-category* number of unique agents and unique data points. This validates that the selected airports widely vary in traffic density and overall crowedness. The table includes additional information such as the month from which we sampled the data, and data quality in terms of interpolated points and agent type percentages (Interp and Type in Table 1). For instance, out of the ~300M global data points, only 3.46% of the data points were interpolated, suggesting minimal need for interpolation. Finally, while we note that the majority of the unique agents (~83.47%) are classified as *unknown*, we have no control over the agent categorization process, and improvements to such process are out of the scope of our work.

Table 6 Raw trajectory data summary per airport showing the *total* and *per-category* number of unique agents and data points along with the percentage of interpolated points.

Airport	Month	Total		Aircraft		Vehicles		Unknown	
		Num. Agents	Num. Data Points (% Interp.)	Num. Agents (% w.r.t. Total)	Num. Data Points (% Interp.)	Num. Agents (% w.r.t. Total)	Num. Data Points (% Interp.)	Num. Agents (% w.r.t. Total)	Num. Data Points (% Interp.)
PANC	Nov	131.35k	15.43M (0.22%)	16.96k (12.91%)	5.88M (0.15%)	4.01k (3.12%)	2.51M (0.84%)	110.29k (83.97%)	7.035M (0.06%)
KBOS	Jan	94.99k	23.39M (0.62%)	33.44k (35.20%)	14.77M (0.45%)	4.27k (4.50%)	2.94M (1.33%)	57.29k (60.30%)	5.68M (0.68%)
KEWR	Mar	140.81k	30.86M (4.86%)	38.86k (27.59%)	20.81M (5.67%)	2.21k (1.57%)	1.23M (8.32%)	99.75k (70.84%)	8.81M (2.47%)
KDCA	Dec	61.85k	17.78M (9.94%)	25.81k (41.73%)	8.22M (8.29%)	1.30k (2.10%)	1.00M (16.82%)	34.74k (56.17%)	8.56M (10.72%)
KJFK	Apr	645.41k	52.82M (9.89%)	45.15k (6.99%)	28.02M (12.03%)	156 (0.02%)	66.31k (4.66%)	600.11k (92.98%)	24.73M (7.47%)
KLAX	May	451.80k	42.81M (0.49%)	60.24k (13.33%)	24.67M (0.30%)	14.92k (3.30%)	2.79M (3.33%)	376.70k (83.38%)	15.35M (0.27%)
KMDW	Jun	211.92k	28.51M (0.84%)	22.47k (10.61%)	6.69M (0.32%)	6.28k (2.97%)	6.15M (3.35%)	183.22k (86.46%)	15.67M (0.07%)
KMSY	Jul	49.35k	10.37M (0.13%)	10.42k (21.12%)	2.57M (0.08%)	54 (0.11%)	39.89k (3.07%)	38.87k (78.77%)	7.75M (0.13%)
KSEA	Aug	378.54k	38.48M (0.23%)	50.08k (13.23%)	26.13M (0.19%)	290 (0.08%)	274.94k (1.02%)	328.17k (86.70%)	12.077M (0.31%)
KSFO	Sep	185.87k	36.01M (2.91%)	37.36k (20.10%)	16.67M (2.84%)	14.57k (7.84%)	5.65M (3.26%)	133.94k (72.06%)	13.69M (2.87%)
Total		2,351,883	296,448,313 (3.46%)	340,791 (14.49%)	154,436,226 (3.84%)	48,149 (2.05%)	22,653,655 (3.63%)	1,963,086 (83.47%)	119,354,023 (2.95%)

Finally, we validate aircraft motion profiles across airports in Figure 16. Specifically, we focus on (1) heading change in subsequent timesteps, (2) mean speed and (3) mean acceleration per trajectory. We see that speed and heading have an ample spread, reflecting the different aircraft behaviors, e.g., take-off taxiing, vacating, etc. The acceleration profile shows a majority of stationary sequences ($0 m/s^2$ bin), which aligns with the behavior of stationary aircraft awaiting clearance or gate assignment, while the noticeable high deceleration and acceleration profiles correspond to aircraft landing and taking off. While diverse across airports, the speed, acceleration, and heading change follow a similar trend, indicating consistent aircraft behavior and verifying that Amelia-42 accurately captures desired ground operation behaviors.

B. Map Data Analysis.

Table 7 shows that our selected airports also vary at the topological level. First, our selection includes airports with different runway configurations, e.g., *parallel* (P) and *intersecting* (I) runways, and also considering complex topologies

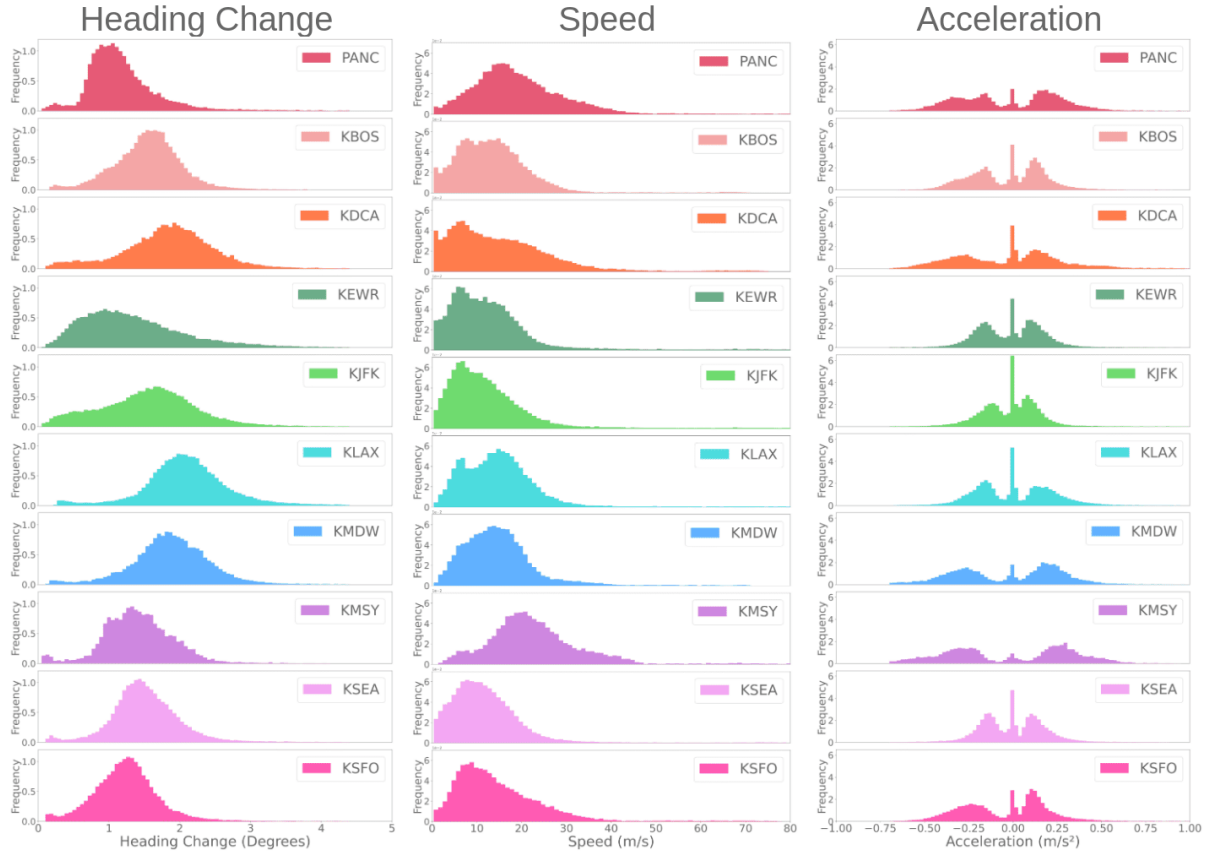


Fig. 16 Aircraft motion profiles, showing a distribution shift across different airports.

Table 7 Map data summary per airport showing runway count and topology, *total* and *per-category* node count. Here, P: parallel, I: intersecting, C: combined runway topology.

Airport	Num. Runways	Runway Topology	Graph Nodes			
			Total	Runway	Taxiways	Hold Line
PANC	3	C	8,016	676	7,134	206
KBOS	5	C	5,056	944	3,826	286
KDCA	3	I	8,154	438	7,590	126
KEWR	3	C	4,804	1,424	3,090	290
KJFK	4	C	7,090	762	5,820	508
KLAX	4	P	10,728	766	9,224	738
KMDW	5	C	4,132	582	3,122	428
KMSY	2	I	1,408	474	790	144
KSEA	3	P	4,782	540	4,000	242
KSFO	4	C	9,032	686	7,992	354

which include various *combinations* (*C*) of both types. We also summarize each airport’s graph. We show the *total* and *per-category* number of nodes in each graph. From these numbers, we can contrast the relative complexity between maps, e.g., a *low-complexity* map such as *KMSY* which only has ~1.5k nodes vs. a *high-complexity* one like *KLAX* with

~11k.

C. Experiment Family Details

We consider topological diversity and the crowdedness scale to determine the `MultiAirport` order. For topological diversity, we focus on the runway organization (see Table 7), and we use the number of unique data points as a proxy for the crowdedness scale level (see Table 6). In the list below, we summarize the selection per experiment, i.e., the airports that get removed from the training set. In parentheses, we include the airport’s runway topology (P: parallel, I: intersecting, and C: combined) and scale rank from 1 (lowest) to 10 (highest).

- `10-Seen`: We include all airports, i.e., all topology types and scales. Here, 6 airports have combined topologies, 2 intersecting runways only, and 2 parallel runways only.
- `7-Seen`: We remove one airport per topology type from `10-Seen`: `KLAX` (P, 9), `KMSY` (I, 1), `KJFK` (C, 10).
- `4-Seen`: We remove one airport per topology type from `7-Seen`: `KSEA` (P, 8), `KDCA` (I, 3), `PANC` (C, 2). All of the remaining airports have combined topology and a variety of scales to ensure interaction diversity.
- `3-Seen`: We remove the largest-scale airport from `4-Seen`, `KSFO` (C, 7).
- `2-Seen`: We remove the smallest-scale airport from `3-Seen`, `KBOS` (C, 4).
- `1-Seen`: We remove the largest-scale airport from `2-Seen`, `KEWR` (C, 6). The only seen airport is `KMDW` (C, 5).

E. Amelia-TF Supplementary

This section provides additional details about our scene representation and analyses to justify our design. We provide model implementation details and prediction visualization for one of our models showcasing generalization capabilities.

A. Scene Representation

We follow an ego-centric scene representation where all agent trajectories and contexts in a scene are encoded w.r.t. to a pre-selected *ego-agent*. We aim to characterize *safety-relevant* behaviors and interactions within airport operations such as aircraft preparing for take-off, stationary aircraft near hold-short lines, aircraft landing, and taxiing out. To streamline our focus on critical interactions, we developed a selection method inspired by previous work [48, 54], which identifies relevant ego-agents and produces complex scene representations.

An overview and toy example of our scene representation and ego-agent selection methodology is shown in Figure 17. The example depicts a scene with a variety of behaviors: an aircraft landing on a **runway**, two aircraft vacating a **taxiway**, an aircraft waiting near a **hold-short line**, and two vehicles. To select the most relevant agents, our method takes each agent’s trajectory and map information and computes a score indicating how *critical* it is; where the higher the score, the more critical the agent is deemed. Our score, specifically, is the result of a function describing each agent’s *kinematic* and *interaction* profiles as in [48].

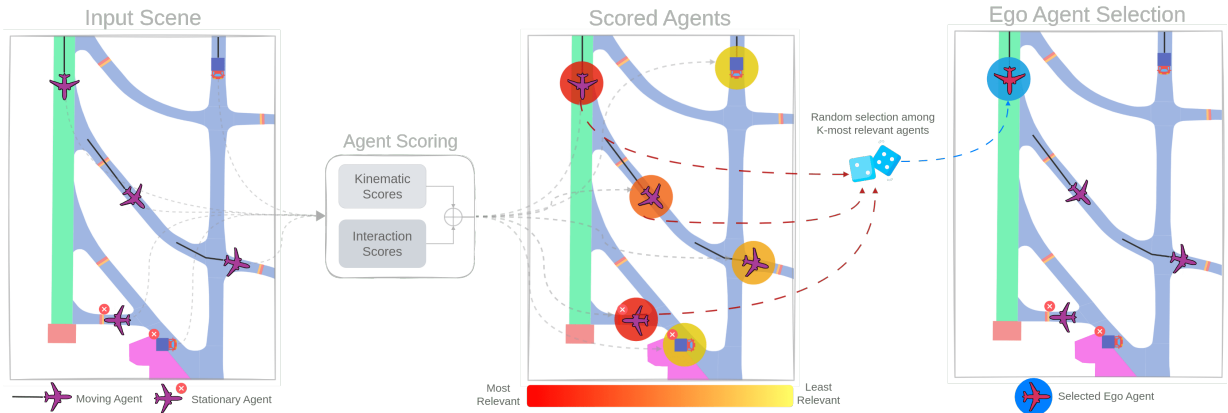


Fig. 17 Overview of our scene representation methodology. Given an input scene consisting of N agents, we compute a *kinematic* and *interactive* score for each agent. To represent the final scene, we keep the K -highest scored agents, and randomly select an ego-agent among them.

We then select the K -most critical agents to represent the final scene. Next, we randomly choose the ego-agent, e , among the selected agents and transform the scene w.r.t. its pose at the last observed timestep, $\mathbf{x}_{t_o}^e$. The final transformed trajectories, $\mathbf{x}_{t_o-H:t_o} \in \mathbb{R}^{K \times H \times D}$, and corresponding historical context, $\mathbf{c}_{t_o-H:t_o} \in \mathbb{R}^{K \times H \times P \times C}$, are encoded using two MLP, ϕ^x and ϕ^c , respectively.

B. Implementation Details

Computational Details. We trained all of our models on shared servers equipped with an AMD Ryzen Threadripper PRO 5955WX CPU and a single NVIDIA 4090 RTX GPU.

Scene Representation. As explained earlier, we consider $T = 60$ seconds scenes to capture long-horizon interactions, where the first $H = 10$ seconds are the historical segment and the remaining $F = 50$ seconds are for prediction to encourage long-horizon and preemptive reasoning from minimal historical information. Agents whose trajectories are shorter than T , e.g., agents that exit the scene earlier, or enter it later, are padded with zeroes. The scene length selection was determined empirically, but as we will show in our scene visualizations, it is sufficient to capture long-horizon and diverse maneuvers.

Agent Selection. For the **kinematic** state, we encode the agent’s speed, acceleration, and jerk profiles. We also account for stationary and slow-moving agents near hold-short lines, which are regions where an aircraft should stop before entering a runway. These are especially important since they help ensure an aircraft’s proper positioning. To characterize these situations, we incorporate a waiting interval measure weighted by the inverse of the distance to the hold line. For the **interaction** state, we consider each agent pair and compute a loss of separation value as in [16], their minimum time to the conflict point as in [48].

For a given scene, we select a maximum of $K = 5$ agents as the *relevant* agents following the selection process described in Section E.A. We obtain each selected agent’s local context consisting of the $P = 100$ closest points to their location at the last observed timestep. Through this scheme, we obtain over **19.2M scenes**, comprising **~158.2M sequences** or **9.4B tokens**, where each token represents an agent’s state at a given timestep.

Agent Feature Extractor. The final transformed trajectories are encoded using a 3-layer MLP with positional embedding.

Context Feature Extractor. We follow *VectorNet* [32] to encode map information. Our model encodes individual local patches for each agent in the scene, in contrast to prior works where a shared global context is used for all agents in the scene [32, 35, 37]. The intuition behind it is that, in aviation, relevant interactions are not necessarily local as would often be the case for settings such as autonomous driving or navigation in human crowds. For instance, while an autonomous vehicle might be more interested in potential interactions with vehicles at a nearby intersection or conflict region, an aircraft might be interested in the potential interaction with an agent at the other end of the runway. In our domain, however, encoding the global airport map information in the scene may make it difficult for the model to generalize to unseen settings. Thus, we opt for a local context encoding and assume that relative distances between agents and context regions are preserved in the ego-centric scene transformation.

Scene Encoder. Our trajectory forecasting model follows a transformer-based architecture that uses a factorized attention scheme for efficient computations as in [37]. The model maintains a $K \times F \times D$ representation across all transformer layers while interleaving two types of self-attention layers: a *temporal* and an *interaction* one, as well as a *context* cross-attention layer as shown in Figure 5. For brevity, we refer to a block comprising these three layers subsequently as TIC.

The **temporal** layer is designed as a causal transformer [55] used for learning the time-wise dependencies within trajectories. It does so by attending to past features across the time dimension using a mask operator, \mathbf{M} , that only *looks* at the previous states from a given timestep. Then, the **interaction** layer is designed to learn agent-to-agent relationships by attending over the features across the agent dimension. We implement both of these layers as multi-head attention (MHA) blocks [56] which receive the joint feature from the previous layer, as the query, key, and value parameters.

The **context** cross-attention layer is then used to exploit the relationships between agent and map features. This layer is also implemented as a MHA block, however, using agents’ joint feature as the query input, while the keys and values are obtained from the embedded context.

Trajectory Decoder. To model the distribution of possible futures for a scene, we adopt a Gaussian Mixture Model (GMM) following [35, 50] modeled as a 2-layer MLP that receives the output feature at the final layer of the scene encoder and produces an output representing the agents’ predicted means and covariances with an associated likelihood for the F future timesteps.

Model details. We use a 5-layer MLP with layer normalization to extract agent features and a 4-layer MLP with batch normalization to extract context features. Our scene encoder is built using 3 TIC blocks that sequentially combine. Each layer in the block consists of an MHA module with $h = 8$ attention heads and a 5-layer MLP that outputs the final feature embeddings. Our GMM is built as a 2-layer MLP with a GELU activation and produces $M = 4$ output heads. The hidden dimensions of all MLPs are of size $D = 256$. The final model comprises **~89.8M parameters**. We train it for at most 100 epochs and use a standard Adam optimizer with a learning rate of $lr = 1e - 4$. Full details are shown in Table 8.

C. Trajectory Forecasting Results

Figure 18 depicts qualitative examples for 7-Seen, showing *seen* (left column) and *unseen* (right column) airports. In particular, the figure shows the model’s predictions on four common aircraft operations: take-off roll (first row), landing (second), vacating a runway upon landing (third), and taxiing in preparation for take-off (fourth). Through varying airport topologies and agent distributions within the map, these results show that *Amelia-TF* is able to make strong long-term predictions for each of the tasks in both settings.

Table 8 Architecture of *Amelia*, inspired by [32, 37]. Here $T = 60, K = 5, D_x = 4, D_c = 7, D_e = 256, D_f = 7$.

Module	Input(s)	Output	Layer Type	Operation Description	Output Dimensions	Num. Parameters
Agent Feature Extractor ϕ^x	\mathbf{x}	a_1	Linear	–	$K \times T \times D_x$	1.3K
	a_1	a_2	LayerNorm	–	$K \times T \times D_e$	512
	a_2	a_3	ReLU	–	$K \times T \times D_e$	–
	a_3	$\bar{\mathbf{x}}$	Linear	–	$K \times T \times D_e$	65.8K
		PE	Embedding	Time embedding	$K \times T \times D_e$	15.4K
	$\bar{\mathbf{x}} + \text{PE}$	$\bar{\mathbf{x}}_{\text{PE}}$	Linear	–	$K \times T \times D_e$	65.8K
Context Feature Extractor ϕ^c	\mathbf{c}	c_1	Linear	–	$K \times P \times D_c$	1.5K
	c_1	c_2	BatchNorm	–	$K \times P \times D_e$	200
	c_2	c_3	ReLU	–	$K \times P \times D_e$	–
	c_3	c_4	Linear	–	$K \times P \times D_e$	65.8K
	c_4	c_5	BatchNorm	–	$K \times P \times D_e$	200
	c_5	c_6	ReLU	–	$K \times P \times D_e$	–
	c_6	c_7	Linear	–	$K \times P \times D_e$	81.9K
	c_7	c_8	BatchNorm	–	$K \times P \times D_e$	6.4K
	c_8	c_9	ReLU	–	$K \times P \times D_e$	–
	c_9	$\bar{\mathbf{c}}$	Linear	Feature down-projection	$K \times T \times D_e$	819K
Scene Encoder	$\bar{\mathbf{x}}_{\text{PE}}$	e_1	Transformer	Self-attention across T	$K \times T \times D_e$	789K
	e_1	e_2	Transformer	Self-attention across K	$K \times T \times D_e$	789K
	$e_2, \bar{\mathbf{c}}$	e_3	Transformer	Cross-attention	$K \times T \times D_e$	789K
	e_3	e_4	Transformer	Self-attention across T	$K \times T \times D_e$	789K
	e_4	e_5	Transformer	Self-attention across K	$K \times T \times D_e$	789K
	$e_5, \bar{\mathbf{c}}$	e_6	Transformer	Cross-attention	$K \times T \times D_e$	789K
	e_6	e_7	Transformer	Self-attention across T	$K \times T \times D_e$	789K
	e_7	e_8	Transformer	Self-attention across K	$K \times T \times D_e$	789K
	e_8	e_9	Linear	Refinement Layer	$K \times T \times D_e$	525K
Scene Decoder	e_9	d_1	Linear	–	$M \times K \times T \times D_e$	16.6K
	d_1	d_2	GeLU	–	$M \times K \times T \times D_e$	–
	d_2	μ_x, Σ_x, ρ	Linear	–	$M \times K \times T \times D_f$	1.8K
	ρ	ρ	Softmax	Softmax across M	$M \times K \times T \times 1$	–

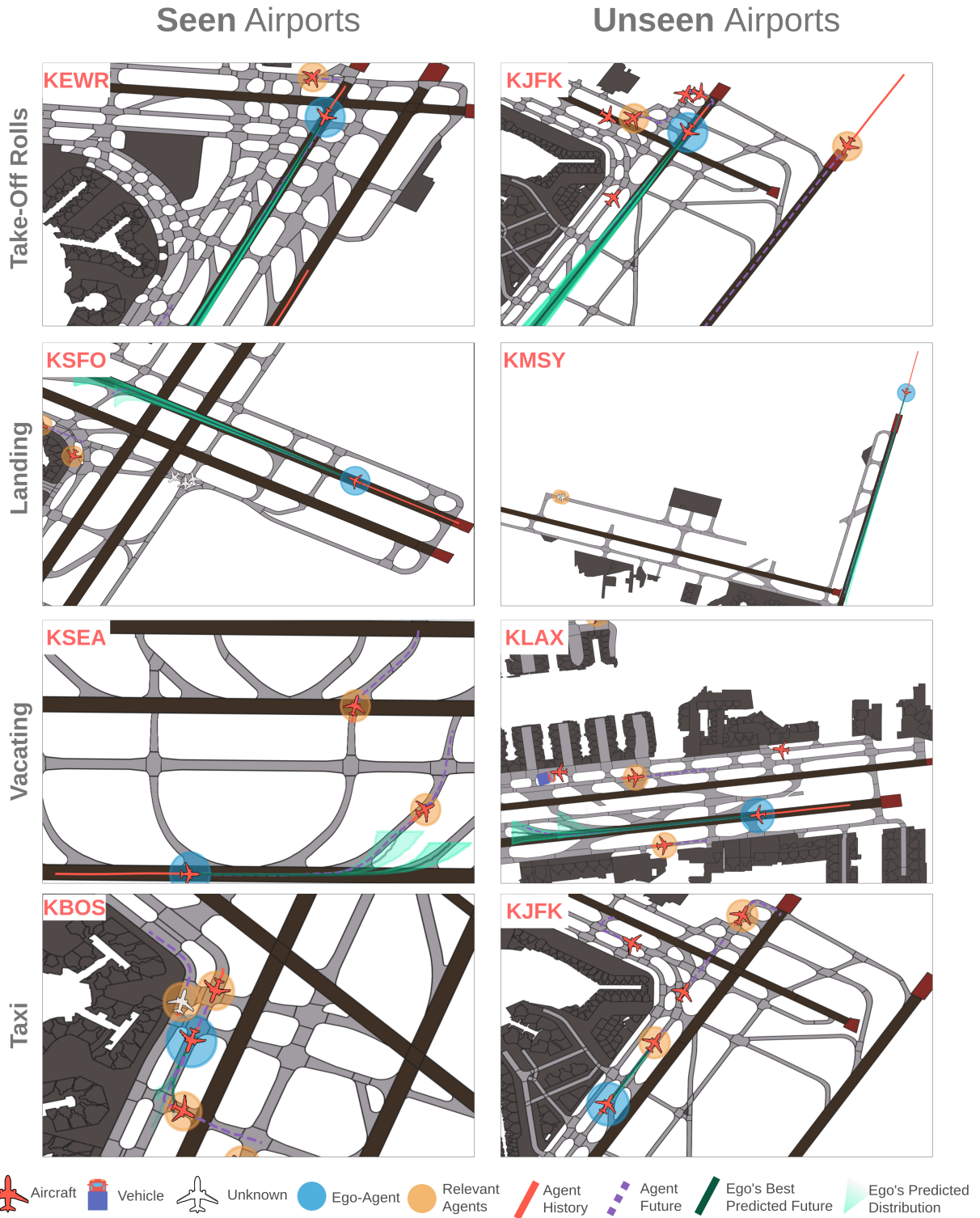


Fig. 18 Prediction results for the 7-Seen experiment on four different tasks: take-off roll, landing, vacating a runway, and taxiing. We compare long-horizon ($F = 50s$) predictions for *seen* (left) and *unseen* airports (right).

D. Scenario Representation Strategy Validation

We study whether our scene selection strategy (Critical) produces more complex and critical interactions by comparing it against a baseline selection approach in which K agents are randomly chosen to represent a scene (Random). As proxies for these components, we analyze the percentage of stationary agents selected as ego agents, as well as the average closest distance between a given agent in a scene and the closest conflict point.

Table 9 Ego-agent selection statistics for the Random and Critical strategies. In parentheses, we show the relative percentage difference between relevant and random strategies.

Airport	Total Num. Ego-agents	Random Selection Strategy				Critical Selection Strategy			
		Stationary	Avg. Closest Dist. to Conflict Point (m)			Stationary	Avg. Closest Dist. to Conflict Point (m)		
		Ego-agents (%)	All Agents	Stationary Agents	Moving Agents	Ego-agents (%)	All Agents	Stationary Agents	Moving Agents
PANC	481,353	1.84	74.44	74.15	107.87	1.75 (-4.89%)	72.26 (-2.93%)	72.08 (-2.80%)	96.40 (-10.64%)
KBOS	435,162	15.28	82.30	69.43	153.66	11.30 (-26.05%)	70.44 (-14.42%)	60.44 (-12.95%)	148.96 (-3.06%)
KDCA	455,366	43.92	103.48	95.84	113.25	36.84 (-16.12%)	99.61 (-3.74%)	92.25 (-3.74%)	112.23 (-0.90%)
KEWR	195,615	10.58	95.14	92.95	113.62	7.97 (-24.67%)	83.29 (-12.45%)	81.40 (-12.43%)	105.12 (-7.49%)
KJFK	54,458	38.29	88.30	78.38	104.27	30.60 (-20.08%)	74.79 (-15.30%)	68.42 (-12.71%)	89.23 (-14.43%)
KLAX	125,602	5.26	50.55	49.24	74.04	4.27 (-18.82%)	47.01 (-6.99%)	46.52 (-5.53%)	58.15 (-21.47%)
KMDW	268,734	9.49	66.58	70.54	28.84	9.91 (4.43%)	58.14 (-12.69%)	61.93 (-12.21%)	23.69 (-17.86%)
KMSY	673,439	17.69	147.63	149.73	137.85	17.87 (1.02%)	144.20 (-2.32%)	146.11 (-2.42%)	135.41 (-1.77%)
KSEA	85,948	4.51	81.19	79.17	124.06	3.24 (-28.16%)	77.57 (-4.45%)	76.15 (-3.81%)	120.03 (-3.25%)
KSFO	186,436	26.22	82.76	78.19	95.62	20.70 (-21.05%)	68.25 (-17.54%)	65.34 (-16.44%)	79.42 (-16.95%)
Average	296,211	17.31	87.24	83.76	105.31	14.45 (-15.44%)	79.55 (-9.28%)	77.06 (-8.50%)	96.86 (-9.78%)

Note: The percentage of stationary agents and the average closest distance to a conflict point are reported for the test set.

Table 9 summarizes the per-airport ego-agent selection statistics for both strategies. Each column in **Critical**, shows in parentheses the average percentage change w.r.t. **Random**. Overall, we show that **Critical** generally selects agents with more dynamic profiles as depicted by the **15%** average reduction for the percentage of selected stationary ego agents. The table further shows that our strategy selects more agents on average **10%** closer to conflict regions.

We compare qualitative results in Figure 19. We show paired scenes for various airports depicting all agents in the scene, the (K-1)-relevant agents (orange halo), and the selected ego agent (blue halo). This figure shows that our selection strategy often selects more dynamic agents, e.g., aircraft preparing for take-off or landing, and agents in conflicting regions, e.g., aircraft vacating a taxiway. Moreover, the agent-to-agent relationships between the selected relevant agents within our strategy are generally more critical. For example, our strategy often selects aircraft that are either vacating or potentially crossing through a runway soon to be used by another aircraft preparing for take-off. In contrast, the random strategy more often selects less dynamic, non-critical agents.

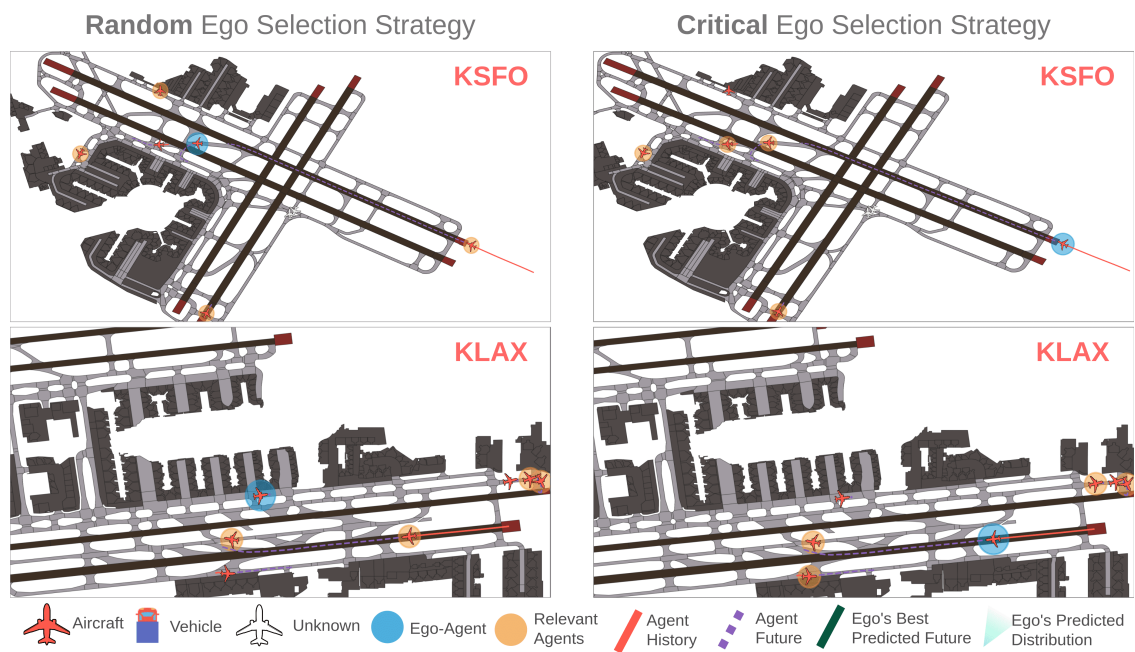


Fig. 19 Scene representation and prediction results for the Random and Critical scene representation strategies, showing that the proposed strategy generally selects agents with a more relevant kinematic and interactive profile.